
Doctoral Dissertations

Student Theses and Dissertations

Summer 2018

Monitoring of hybrid manufacturing using acoustic emission sensor

Haythem Gaja

Follow this and additional works at: https://scholarsmine.mst.edu/doctoral_dissertations



Part of the [Mechanical Engineering Commons](#)

Department: **Mechanical and Aerospace Engineering**

Recommended Citation

Gaja, Haythem, "Monitoring of hybrid manufacturing using acoustic emission sensor" (2018). *Doctoral Dissertations*. 2701.

https://scholarsmine.mst.edu/doctoral_dissertations/2701

This thesis is brought to you by Scholars' Mine, a service of the Missouri S&T Library and Learning Resources. This work is protected by U. S. Copyright Law. Unauthorized use including reproduction for redistribution requires the permission of the copyright holder. For more information, please contact scholarsmine@mst.edu.

MONITORING OF HYBRID MANUFACTURING USING ACOUSTIC EMISSION
SENSOR

by

HAYTHEM GAJA

A DISSERTATION

Presented to the Faculty of the Graduate School of the
MISSOURI UNIVERSITY OF SCIENCE AND TECHNOLOGY

In Partial Fulfillment of the Requirements for the Degree

DOCTOR OF PHILOSOPHY

in

MECHANICAL ENGINEERING

2018

Approved by

Frank Liou, Advisor
K. Chandrashekhara
Edward Kinzel
Heng Pan
Elizabeth Cudney

© 2018

Haythem Gaja

All Rights Reserved

PUBLICATION DISSERTATION OPTION

This dissertation has been prepared in the format of the publication option. Three journal articles are presented.

Paper I, Pages 4 to 37 “Automatic Detection of Depth of Cut during End Milling Operation Using Acoustic Emission Sensor” is in the style required by International Journal of Advanced Manufacturing Technology. It has been accepted and published. The citation is: Gaja, Haythem, Liou, Frank, (2016). Automatic Detection of Depth of Cut during End Milling Operation Using Acoustic Emission Sensor. international Journal of Advanced Manufacturing Technology 86 (2016) 2913-2925.

Paper II, Pages 38 to 66 “Defects Monitoring of Laser Metal Deposition Using Acoustic Emission Sensor” is in the style required by International Journal of Advanced Manufacturing Technology. It has been accepted and published. The citation is: Gaja, Haythem, Liou, Frank, (2017). Defects Monitoring of Laser Metal Deposition Using Acoustic Emission Sensor. international Journal of Advanced Manufacturing Technology 90 (2017) 561-574.

Paper III, Pages 67 to 98 “Defects Classification of Laser Metal Deposition Using Logistic Regression and Artificial Neural Networks for Pattern Recognition” is in the style required by International Journal of Advanced Manufacturing Technology. It has been accepted and published. The citation is: Gaja, Haythem, Liou, Frank, (2018). Defects Classification of Laser Metal Deposition Using Logistic Regression and Artificial Neural Networks for Pattern Recognition. International Journal of Advanced Manufacturing Technology 94.

ABSTRACT

The approach of hybrid manufacturing addressed in this research uses two manufacturing processes, one process builds a metal part using laser metal deposition, and the other process finishes the part using a milling machining. The ability to produce complete functioning parts in a short time with minimal cost and energy consumption has made hybrid manufacturing popular in many industries for parts repair and rapid prototyping. Monitoring of hybrid manufacturing processes has become popular because it increases the quality and accuracy of the parts produced and reduces both costs and production time. The goal of this work is to monitor the entire hybrid manufacturing process. During the laser metal deposition, the acoustic emission sensor will monitor the defect formation. The acoustic emission sensor will monitor the depth of cut during milling machining. There are three tasks in this study. The first task addresses depth-of-cut detection and tool-workpiece engagement using an acoustic emission monitoring system during milling machining for a deposited material. The second task, defects monitoring system was proposed to detect and classify defects in real time using an acoustic emission (AE) sensor and an unsupervised pattern recognition analysis (K-means clustering) in conjunction with a principal component analysis (PCA). In the third task, a study was conducted to investigate the ability of AE to detect and identify defects during laser metal deposition using a Logistic Regression Model (LR) and an Artificial Neural Network (ANN).

ACKNOWLEDGMENTS

I would like to express my gratitude to the people, without the decisive contribution of whom the completion of this dissertation would not be possible, throughout my stay here at Missouri University of Science and Technology. I would like to express my deepest gratitude to my advisor Dr. *Frank*, who gave me an opportunity to conduct research under his supervision. Dr. *Frank* has continuously conveyed a passion for research work and excitement for teaching.

I owe thanks and deep appreciation also to Dr. K. Chandrashekhara, Dr. Edward Kinzel, Dr. Heng Pan, and Dr. Elizabeth Cudney for their time and service on the Advisory Committee.

I would like to show my gratitude to family here and my parents and siblings in my home country, for that has guided and supported me in all aspects of my life. It was under their supervision that I gained the ability to tackle challenges and issues. A special thanks to all my dear friends who have been supporting me throughout my life with their love, and encouragement.

TABLE OF CONTENTS

	Page
PUBLICATION DISSERTATION OPTION	ii
ABSTRACT	iv
ACKNOWLEDGMENTS	v
LIST OF ILLUSTRATIONS	ix
LIST OF TABLES	xii
 SECTION	
1.INTRODUCTION	1
 PAPER	
I. AUTOMATIC DETECTION OF DEPTH OF CUT DURING END MILLING OPERATION USING ACOUSTIC EMISSION SENSOR	4
ABSTRACT	4
1. INTRODUCTION	5
2. EXPERIMENTS AND DATA COLLECTION	9
3. RESULTS AND DISCUSSION	15
3.1. ANALYSIS OF VARIANCE (ANOVA)	15
3.2. REGRESSION BASED MODELING	16
3.3. ARTIFICIAL NEURAL NETWORK BASED MODELING	19
4. ESTIMATION OF DEPTH-OF-CUT	24
5. CONCLUSIONS	31
6. FUTURE WORK	31
APPENDIX	33

REFERENCES	35
II. DEFECTS MONITORING OF LASER METAL DEPOSITION USING ACOUSTIC EMISSION SENSOR.....	38
ABSTRACT.....	38
1. INTRODUCTION	39
2. EXPERIMENTS AND DATA COLLECTION	42
3. RESULTS AND DISCUSSION.....	48
3.1 PRINCIPAL COMPONENT ANALYSIS	48
3.2. CLUSTERING ANALYSIS	53
3.3. DEFECTS TYPES AND OPTICAL MICROSCOPY STUDY	62
4. CONCLUSIONS.....	64
ACKNOWLEDGMENT.....	65
REFERENCES	65
III. DEFECTS CLASSIFICATION OF LASER METAL DEPOSITION USING LOGISTIC REGRESSION AND ARTIFICIAL NEURAL NETWORKS FOR PATTERN RECOGNITION	67
ABSTRACT.....	67
1. INTRODUCTION	68
2. EXPERIMENTS AND DATA COLLECTION	72
3. RESULTS AND DISCUSSION.....	81
3.1. LOGISTIC REGRESSION-BASED MODELING.....	81
3.2. ARTIFICIAL NEURAL NETWORK BASED MODELING.....	82
3.3. MODELS VERIFICATION (DEFECTS CLASSIFICATION).....	88
4. CONCLUSIONS.....	95
ACKNOWLEDGMENT.....	96
REFERENCES	96

SECTION

2. CONCLUSIONS.....	99
BIBLIOGRAPHY.....	100
VITA.....	102

LIST OF ILLUSTRATIONS

	Page
PAPER I	
Figure 1. Experimental setup	10
Figure 2. Tool wear for end mill tool.....	11
Figure 3. Tool wear of 320 μ m	12
Figure 4. Typical Taylor tool wear curve	12
Figure 5. A sample of acoustic emission and the RMS signals	14
Figure 6. 3D-surface plot with scatter plot of RMS for all factors combination	17
Figure 7. Quantile-quantile plot for RMS residuals.....	19
Figure 8. Sigmoid activation function	20
Figure 9. Neural network architecture	22
Figure 10. Neural network performance.....	24
Figure 11. Depth-of-cut estimation.....	25
Figure 12. Interrupted cutting (a) nominal/estimated depth-of-cut (b) cutting geometry	26
Figure 13. Inclined surface cutting (a) nominal/estimated depth-of-cut (b) cutting geometry	27
Figure 14. Scanning the part before machining.....	28
Figure 15. The coordinate reference system using three points.....	29
Figure 16. Machined material slicing (a) first section. (b) fifteenth section.....	30
Figure 17. Measured and detected depth-of-cut for a deposited material.....	30

PAPER II

Figure 1. Experimental setup shown the LMD system and AE data acquisition system.....	42
Figure 2. Optical image of the metal powders used in deposition process.....	43
Figure 3. Step-by-step operations used to perform the acoustic emission analyses	45
Figure 4. AE raw signal acquired during LMD process	46
Figure 5. Time dependent AE event features.....	48
Figure 6. Time-dependent AE event features	53
Figure 7. Silhouette width value for the events in the two clusters	56
Figure 8. Principal component projection and clusters distribution for the AE events.....	58
Figure 9. Comparing the features in clusters one and two the AE events	60
Figure 10. Comparison between the waveforms from both clusters	61
Figure 11. Optical image of a transverse cross-sectioned laser deposit showing a crack and gas porosity	62
Figure 12. Optical image of a transverse cross-sectioned laser deposit showing a gas porosity	63

PAPER III

Figure 1. Experimental setup shown the LMD system and AE data acquisition system.....	72
Figure 2. Optical image of the metal powders used in deposition process.....	74
Figure 3. Time dependent AE event features.....	76
Figure 4. Step-by-step operations used to perform the acoustic emission analyses	80
Figure 5. Sigmoid activation function	83

Figure 6. Neural network architecture	84
Figure 7. Neural network performance	86
Figure 8. AE raw signal acquired during LMD process	88
Figure 9. Comparing the signal features between crack and porosities.....	92
Figure 10. Comparison between the waveforms emitted by cracks and porosities	93
Figure 11. Optical image of a transverse cross-sectioned laser deposit showing a crack	94
Figure 12. Optical image of a transverse cross-sectioned laser deposit showing a gas porosity	94

LIST OF TABLES

	Page
PAPER I	
Table 1. Factors and levels defined for experimentation	14
Table 2. Results of the analysis of variance.....	15
Table 3. Results of the regression analysis	18
PAPER II	
Table 1. The composition and thermal properties of titanium and tool steel metallic powders (mass %).	44
Table 2. Laser metal deposition process parameters	45
Table 3. Time domain and frequency domain AE signal features.....	47
Table 4. Standardized of the AE signal features.....	50
Table 5. Eigenvalues of the seven AE signal features	52
Table 6. Average silhouette width for different number of clusters	55
Table 7. Cluster centers.....	57
Table 8. Cluster membership	57
Table 9. Analysis of variance (ANOVA) of the cluster centers and features importance.....	59
PAPER III	
Table 1. The composition and thermal properties of titanium and tool steel metallic powders (mass %).	74
Table 2. Time domain and frequency domain AE signal features.....	75
Table 3. Laser metal deposition process parameters	77

Table 4. Standardized AE signal features and the clustering results 78

Table 5. Results of the regression analysis 81

Table 6. Results of the logistic regression and neural network analysis 87

Table 7. Verification results of the logistic regression analysis and neural
network 89

SECTION

1. INTRODUCTION

The scope of this project is to monitor the entire hybrid manufacturing process, which consists of laser metal deposition and CNC milling machining using acoustic emission sensor to produce defect-free parts with accurate dimension and high quality. During the laser metal deposition, the acoustic emission sensor detects the defect formation. On the other hand, the acoustic emission sensor monitors the depth of cut during milling machining. Automation of manufacturing processes has become popular because it increases the quality and accuracy of the parts produced and reduces both costs and production time. However, automated manufacturing of metallic structures has thus far been limited to determination of the building sequence, optimization and evaluation of the feasibility of direction of the machining process. The aim of this research is to develop a novel perspective towards the monitoring strategies involved in laser metal deposition and milling machining. The ultimate goal is to develop an online monitoring system that can be integrated into any laser metal deposition hybrid system to support an effective monitoring system.

This research will result in a new understanding of the interaction between the acoustic emission signal on one side and depth of cut and the laser metal deposition defects on the other side. The effects of defects formation on the features of the acoustic emission signal was studied. The variation in the depth of cut and its influence on

acquired signal was analyzed. Different statistical and machine learning techniques were integrated to construct a complete mentoring system for hybrid manufacturing system.

Laser metal deposition is one of powder-based laser deposition additive manufacturing techniques such as laser cladding [1, 2], laser direct casting [3, 4], direct metal deposition [5], directed light fabrication [6-8], laser forming [9], shape deposition manufacturing [10], laser engineered net shaping [11,12], free-form laser consolidation [13,14], and many others. The main process parameters of LMD; laser power, travel velocity, and powder flow rate control the geometry accuracy and the mechanical properties of the finished part by determining the size of the molten pool, the part deformation, and the microstructure of the deposited layers. They affect the temperature profile and cooling rate in the molten pool, as well as the thermal cycles at each location of the fabricated part [15].

The AE technique is one of most powerful monitoring technologies; it has been used for monitoring in many manufacturing processes such as the cutting operations [16-18] and the welding processes. Siracusano [19] propose a framework based on the Hilbert–Huang Transform for the evaluation of material damages, this framework facilitates the systematic employment of both established and promising analysis criteria, and provides unsupervised tools to achieve an accurate classification of the fracture type. Bianchi [20] suggested a wavelet packet decomposition within the framework of multiresolution analysis theory is considered to analyze acoustic emission signals to investigate the failure of rail-wheel contact under fatigue and wear study. The application was shown to be adequate for analyzing such signals and filtering out their noise real-time monitoring. However, more research needed to develop a technique in using AE as a

reliable measure for defect detection of laser metal deposition and depth of cut and tool engagement monitoring during milling machining. A complete system includes:

- Acoustic emission sensor to acquire the AE signal during laser metal deposition and milling machining
- Data acquisition card able to acquire high-frequency signal (1 KHz to 1 MHz)
- Digital microscopic camera to detect the milling tool status without disengaging the tool from the tool holder
- Computer to record the AE signal analysis.
- Oscilloscope to measure the change in the acoustic emission signal over time and it helps in displaying the signal as a waveform in a graph
- An overall integration strategy to achieve the monitoring system

PAPER

I. AUTOMATIC DETECTION OF DEPTH OF CUT DURING END MILLING OPERATION USING ACOUSTIC EMISSION SENSOR

Haythem Gaja ^{*}a, Frank Liou ^a

^a Missouri University of Science and Technology, Mechanical & Aerospace Engineering,
400 W 13th Street, Rolla, MO 65409-0050, USA

ABSTRACT

Any shortfall in the required depth during milling machining can affect the dimensional accuracy of the part produced and can cause a catastrophic failure to the machine. Corrective remedies to fix the dimensions inaccuracy will increase the machining time and costs. In this work, a depth-of-cut monitoring system was proposed to detect depth-of-cut in real time using an acoustic emission sensor and prediction model. The characteristics of the sensor signal obtained in machining processes can be complex in terms of both nonlinearity, and nonstationarity. To overcome this complexity, a regression model and an artificial neural network model were used to represent the relationship between the acoustic emission signal and depth-of-cut. The model was tested under different machining cases and found to be efficient in predicting the depth of cut.

Keywords: Depth of cut Detection, Acoustic emission, artificial neural network

1. INTRODUCTION

One of the difficulties in using an adaptive control and tool monitoring system is an accurate representation of the variation in machining variables such as cutting speed, feed rate, and depth-of-cut. The purpose of monitoring machining process is to prevent and detect damage of tool and/or machined part [1], and to find the optimal set of cutting parameters for the certain machining process [2]. In the end-milling process, particular changes in depth-of-cut must be carefully considered to ensure the effectiveness of the control system.

Many researchers have sought to control surface errors and radial and axial depth-of-cut using analytical models, simulation, force sensors, and other sensors. Choi [3] suggested an algorithm to estimate the cutting depth based on the pattern of cutting force. He found that the cutting force pattern is more useful for this purpose than its magnitude because its pattern reflects the change in cutting depth. However, the magnitude is affected by a number of cutting variables, but not by the depth-of-cut.

Yang [4] suggested an analytical method to identify depth-of-cut variations based on cutting force profile features detected during end milling. Based on the profile characteristics of a single-flute, he studied end mill cutting forces and categorized them into three types. The same study categorized the cutting forces signals of both the single-flute end mill cutting and the multiple-flute end mill cutting based on the cutting process.

Wan [5] predicted the cutting forces and the surface dimensional errors using iteration schemes. Using the finite element method, he devolved a general method to calculate static form errors in peripheral milling of thin-walled structures, and his simulation tool considered the complexity of the workpiece.

Li [6] presented a comprehensive time domain model for general end milling processes. The model measures variations in depth-of-cut using mode forms. The model can also consider additional general conditions such as cutting with a large axial depth-of-cut or small discontinued radial depth-of-cut. In addition to simulating the end milling process this method predicts a number of results for surface profiles and chatter boundaries.

Yonggang [7] examined cutting forces and categorized them into six classes according to a combination of cutting depths, and he proposed a finite-element model to study surface dimensional errors in peripheral milling of thin-walled workpieces for aerospace application. Such error prediction keeps the number of surface errors within permissible bounds.

To forecast a surface form error with the greatest efficiency and accuracy, Yonggang's model relies on a set of flexible, iterative rules with a double iterative algorithm. Prickett [8] presented an approach that uses ultrasonic sensors for online monitoring of depth-of-cut during the end milling processes. The proposed monitoring process tried to contribute to the development of more efficient tool management procedures and supporting infrastructure. However, sensor resolution is an important factor limiting performance.

According to the American Society for Testing Materials acoustic emissions are elastic waves emitted from sources inside a material as a result of the sudden release of energy during metal deformation [9]. Acoustic emissions have been used in many areas, such as tool wear detection and nondestructive testing. Joseph Kaiser was the first to use electronic instrumentation to detect audible sounds produced by metals during

deformation [10]. The acoustic emission wave received by a sensor causes stress [11]. The stress generates an electric field and voltage signal which can be amplified and filtered for further processing. During the deformation in the end milling process, there are several sources of acoustic emission [12] such as; Deformation of work material during cutting, Chipping, breakage, and fracture of cutting inserts. All these sources of acoustic emission are directly proportional to the depth of cut, tool status, cutting speed and feed rate.

A wide range of statistical signal processing methods allow data mining from discretely sampled and random acoustic emission signals. These methods include time domain analysis based on descriptive statistics such as low-order statistical moments, and frequency domain analysis based on the power spectral density (PSD) function. Such methods can be used to extract or characterize particular features of a signal. Ravindra [13] used a statistical method which is a time series modeling technique to extract parameters called *features* to represent the state of the cutting process. He studied autoregressive (AR) parameters and the power of the acoustic emission signal and AR residual signals and found them to be effective in tool condition monitoring. The power of the AR residual signal of the acoustic emissions increases with increases of the flank wear of the cutter during the turning process. Chen [14] proposed a technique based on acoustic emission signal wavelet analysis for tool condition monitoring. His method permits local characterization of the frequency band, which contains the main energy of the signals and depicts this band using wavelet multiresolution analysis. It represents the singularity of the signal using the wavelet resolution coefficient norm. Li and Yuan [15] designed a device to detect acoustic emission signals from a rotating tool. The technique

involves generating features of signals from a wavelet packet transform preprocessor, then associating the preprocessor outputs with the appropriate decisions using a fuzzy clustering method (FCM). Li and Yuan used a wavelet packet transform preprocessor to decompose the signals into different frequency bands in the time domain, and the root mean square values extracted from the decomposed signal of each frequency band were used as a feature. The features most directly related to tool wear are used as final monitoring features.

Recently the AE technique has been used in many machining processes such as milling, turning, and drilling. Duro and Nassehi [1] proposed a multi-sensor data fusion framework for monitoring machining operations based on rotary cutters during milling machining, it found that the AE sensors are indeed highly sensitive to sensor location and to cutting parameters. Zhiqiang [16] presented a tool wear assessment technique in high precision hard turning process using type-2 fuzzy uncertainty estimation on AE signal. The experimental showed that the development trend of uncertainty in acoustic emission signal corresponds to that of cutting tool wear and type-2 fuzzy logic estimation provides the possibility to indicate the uncertainties in AE to monitor tool condition, which could be crucial in maintaining high production quality. Liao [17] discussed a AE based monitoring technique to capture chip formation, penetration depth and cutting malfunctions in bone drilling process. The wavelet energy ratio of AE signal was found to be sensitive to micro-drill penetration depth. It was found the wavelet fractal dimensions of the signal from irregular cutting greatly differ from normal cutting and resulted that the AE signal is associated with the cutting malfunctions and can be adopted to distinguish these irregular events with efficient results.

This work used analysis of variance to determine the significance of factors and their effect on the root mean square (RMS) of the acoustic emission (AE) signal, also a regression model was used to represent the relationship between the AE signal and depth-of-cut, then an Artificial Neural Network (ANN) was constructed for more accurate estimation for depth-of-cut. The output of the sensor and data of cutting conditions and tool status are fed to a neural network to measure operation quality during machining. After the network was trained, the inference system estimated the depth-of-cut in real time from the experimental sensor signal and the cutting conditions. The results of the monitoring algorithm can warn the operator to take the corrective actions to reach the required depth-of-cut. The difference between the desired depth-of-cut and the actual depth-of-cut may be a result of incorrect workpiece set-up, tool length offset change (tool wear), or irregularity of workpiece dimensions. Previous manufacturing processes may also lead to errors in depth-of-cut. For example, when a workpiece is manufactured by laser deposition, forging, or casting, the dimensions are not always accurate and uniform.

2. EXPERIMENTS AND DATA COLLECTION

Figure 1 shows a schematic diagram of the experimental set-up. The milling process was carried out on a Fadal vertical 5-Axis computer numerical control machine (3016L) using a carbide flat-end mill (0.5 in) to cut deposited stainless steel 316 workpieces. The control interface (National Instrument PXI 7240 and PXI 1250) provided the control and data acquisition. An acoustic emission sensor (Kistler 8152B211) captured a high-frequency signal. The bandwidth of the AE sensor was 10 to 1000 kHz. The RMS signals were first fed through the data acquisition system and then

recorded and processed using Labview software. In this study and in other literature [13],[14],[15],[16], [17], it was found that using a single AE sensor without guard sensor is sufficient, where the AE technique has a relatively superior signal-to-noise ratio and sensitivity at the ultra-precision scale, even at extremely low depths of cut [21]. It was found in this study the noise level is much smaller than the signals of interest, also a frequency filtering was used which allowing of passing only those signals falling within a selected bandwidth (500 kHz to 1 MHz). A 500X digital microscopic camera was used to detect tool status without disengaging the tool from the tool holder. The tool condition was documented from the bottom edge radius, which was measured in place with the aid of the vision system.

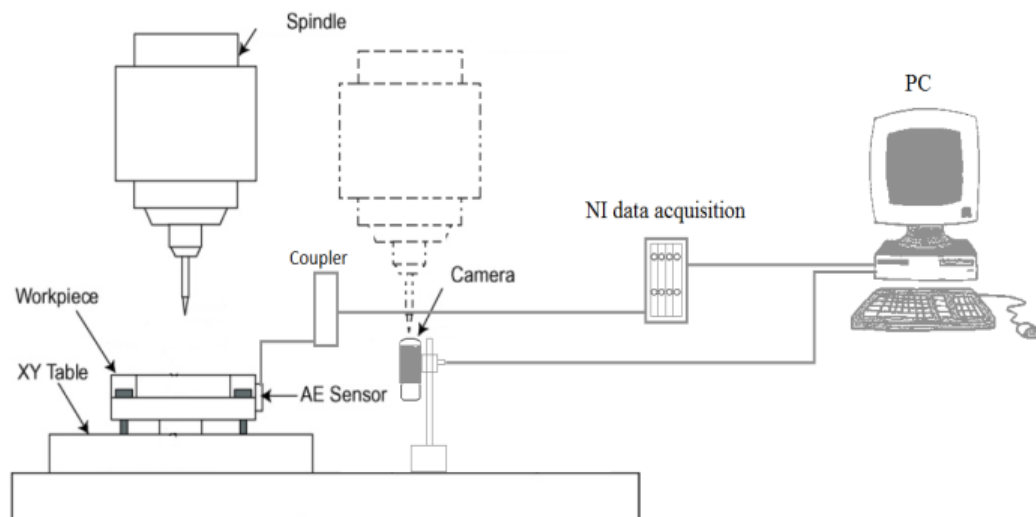


Figure 1. Experimental setup

This study classified tool status according to tool life or tool wear, which is caused by progressive loss of tool material during cutting and which thus changes the

shape of the cutting edge. The tool wear was converted from a pixel scale to micrometer scale. Once the measuring scale was calibrated, tool wear was measured by counting pixels from the vision system and comparing the number with the scale on the reticle. Figure 2 illustrates how the tool wear evaluated using the vision system.

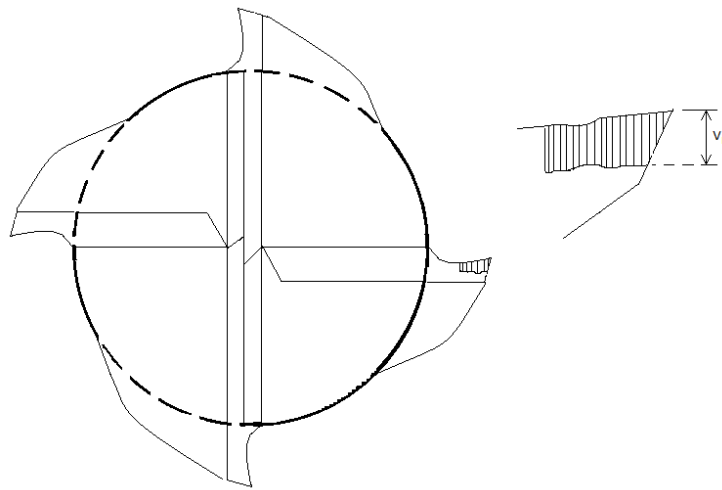


Figure 2. Tool wear for end mill tool

The international organization for standardization [18] recommended that the tool be considered worn-out and reached its end point at $V_B = 0.3$ mm. Here, the output was assigned a value of 1 (for a fresh tool with wear less than $130 \mu\text{m}$), 2 (for an average tool between $130 \mu\text{m}$ and $300 \mu\text{m}$), or 3 (for a worn-out tool with wear greater than $300 \mu\text{m}$). Figure 4 shows a worn-out tool with $320 \mu\text{m}$ tool wear. The tool has four flutes with a different level of wear, so the tool wear value represents an average.

The three tool wear categories were established based on the tool life curve (Taylor tool life curve) which divides the tool life into three stages or regions, initial,

progressive, and severe (see Figure 4). Many features are detectable from a raw acoustic emission signal, such as signal duration, peak amplitude, rise time, and RMS. Feature selection can improve the output.

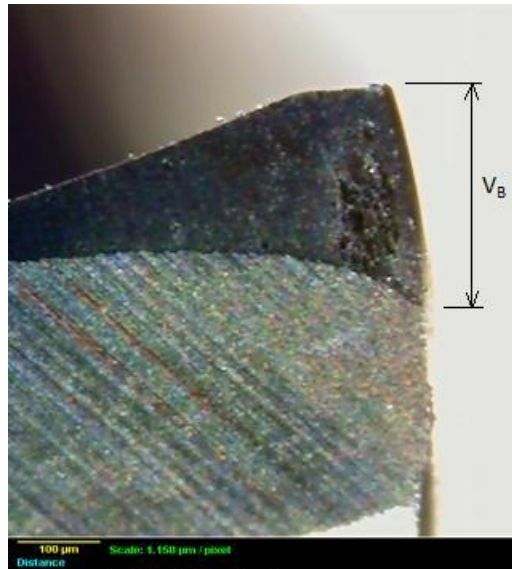


Figure 3. Tool wear of 320 μ m

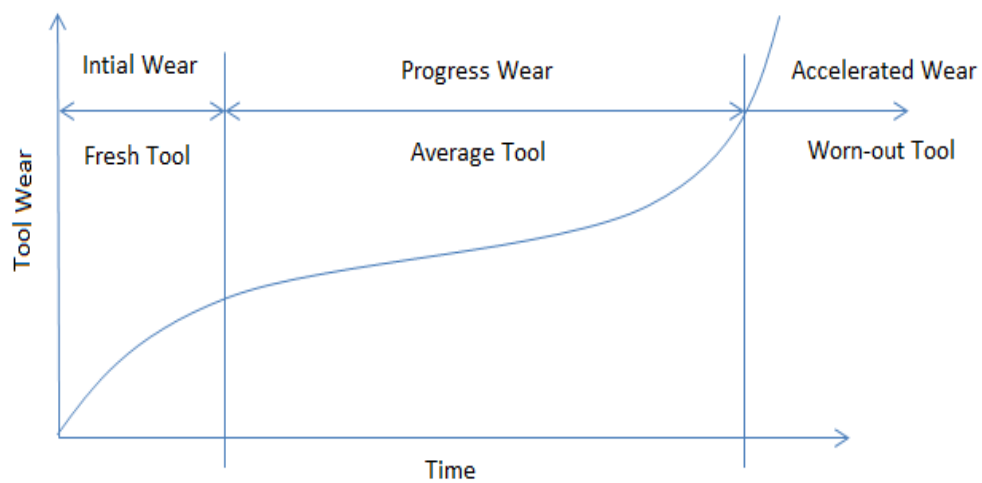


Figure 4. Typical Taylor tool wear curve

Many features are detectable from a raw acoustic emission signal, such as signal duration, peak amplitude, rise time, and RMS. Feature selection can improve the output accuracy and reduce the number of features that must be collected, thus reducing costs [19]. Use of all features is not practical because irrelevant features add noise and complicate the diagnostic task. The root mean square is the square root of the mean value of the squared signal. It is the alternating current voltmeter of the signal and it is always positive. The root mean square is the best way to quantify the energy created by a signal, and it is directly related to the amount of work done by the source that created the signal. It is defined as:

$$RMS = \sqrt{\frac{1}{\Delta T} \int_0^{\Delta T} V^2(t) dt} = \sqrt{\frac{1}{N} \sum_{t=1}^n V^2(t)} \quad (1)$$

Where $V(t)$ represents the signal function or signal value at given time, ΔT is the averaging time or time period, and N is the number of signal values in the time period. Figure 5 shows a sample of acoustic emission and the RMS signals (1 mm depth of cut, 5000 RPM spindle speed and 70 mm/min feed rate)

The experiments described here were designed to investigate the most significant factors affecting the acoustic emission signal during the end milling process. Therefore, their outcomes are significant for the computation of depth-of-cut, and the research considers the cutting tool condition and the cutting variables. These factors include depth-of-cut, spindle speed, feed rate, and tool status.

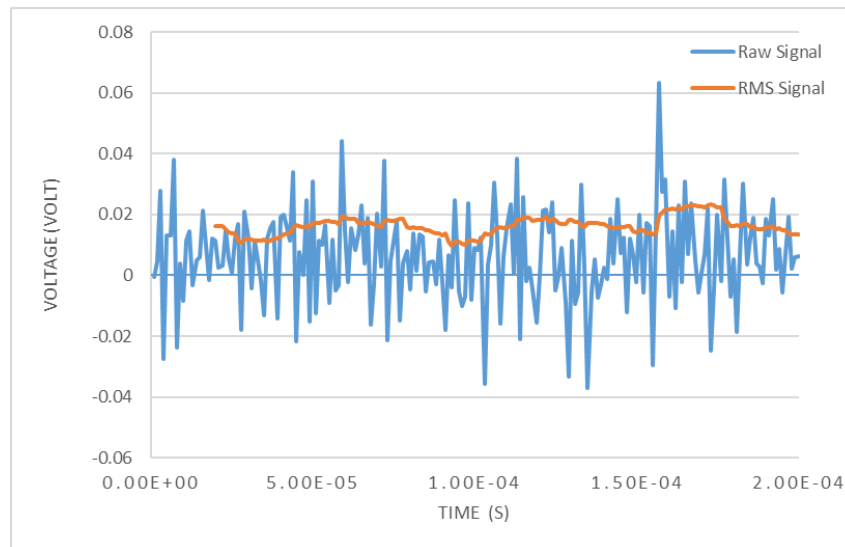


Figure 5. A sample of acoustic emission and the RMS signals

A four factor-three level (3^4) full factorial design experimental design with three replications, a total of 243 cutting tests were run randomly, and a range of cutting conditions were collected. In appendix A, Table 4 shows the average RMS results for full factorial experimental design.

Table 1. Factors and levels defined for experimentation

Depth of cut (mm)	Cutting Speed (RPM)	Feed Rate (mm/round)	Tool Status
0.5	1500	0.01	$\leq 130 \mu\text{m}$
1	3000	0.02	$> 130 \mu\text{m}$ and $\leq 300 \mu\text{m}$
2	5000	0.03	$> 300 \mu\text{m}$

3. RESULTS AND DISCUSSION

3.1. ANALYSIS OF VARIANCE (ANOVA)

Analysis of variance was used to determine the most significant machining parameters among depth-of-cut, cutting speed, feed rate, and tool status that effecting the RMS signal, these factors will be used in the regression model and neural network model. The ANOVA in Table 2 for the response variable (RMS). When the p-value of a specific term (factor) is less than 0.05, then the term is significant, which means that hypothesis of equal means for a given factor can be rejected.

Even though there is 26 % of the variance in the results was not explained by the regression model, the lack of fit error is not significant, most of the error is a pure error that occurs due to natural variation in the process and the regression model accurately fits the data. As can be seen in Table 2, P-value of the model is less than 0.05, this means that the selected factors in the ANOVA explained the variance significantly. Even though there is 26 % of the variance in the results was not explained by the regression model, the lack of fit error is not significant, and the regression model accurately fits the data.

Table 2. Results of the analysis of variance

Source	DF	Sum of Squares	Mean Square	F Value	Pr > F
Regression	8	0.7009	0.0876	25.61	0.032
Residual Error	72	0.2463	0.0034		
Lack of Fit	1	0.0161	0.0161	4.98	0.0603
Pure Error	71	0.2302	0.0032		
Total	80	0.9472			

To better understand the relationship between the machining parameters a 3D-surface plot with scatter plot was constructed as shown in Figure 6. The figure shows the estimated response of RMS varying with a change in the machine parameters. The root mean square of the AE signal is significantly influenced by depth-of-cut followed by tool status, and it is less effected by feed rate. As can be clearly seen in this figure and in the ANOVA, the relationship between the RMS and the interaction of the machine parameters is not linear, for example in Figure 6 (a) the RMS increases as the depth of cut increases and cutting speed decreases and vice versa. In Figure 6 (b) the RMS increases as both depth of cut and cutting speed increase. In Figure 6 (d) The maximum RMS is reached when both cutting speed and feed rate at the lower setting, but the RMS dropped to a minimum value when the cutting speed at the middle setting and feed rate at the higher setting. As a result, in order to predict any of the machining parameters, the model should consider the remaining parameters and their interaction.

3.2. REGRESSION BASED MODELING

The regression model (Table 3) was developed using SAS statistical software, with four independent variables: feed rate, cutting speed, tool status, and the depth-of-cut. The dependent variable was the squared root mean square of the acoustic emission signal. Although this research is sought to estimate depth-of-cut, the data were used to model the squared root mean square.

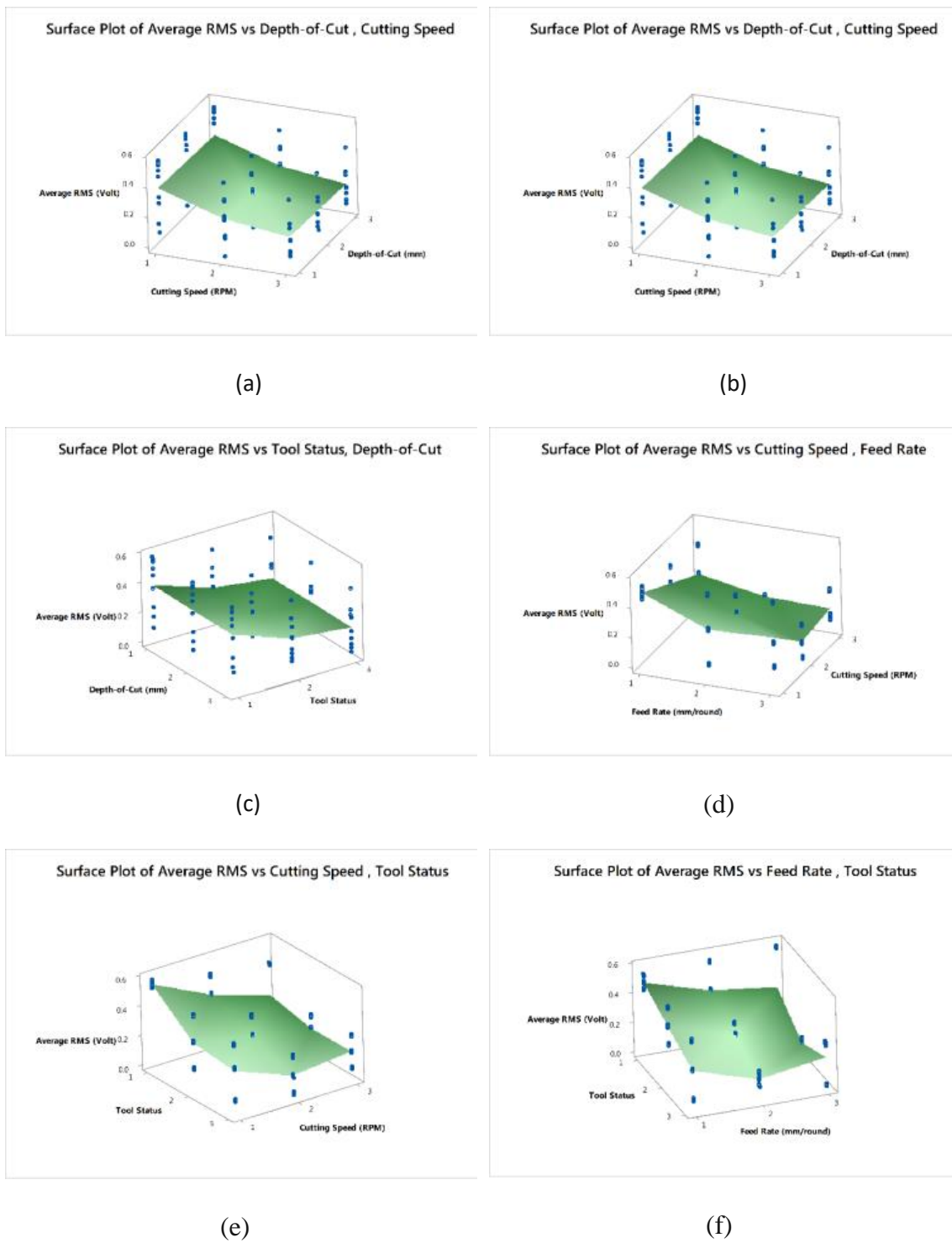


Figure 6. 3D-surface plot with scatter plot of RMS for all factors combination

When an interaction effect is present, that means the impact of one factor depends on the level of the other factor [20]. Interaction does not mean multi-collinearity or correlation, especially that the all factors are significant.

The correlation coefficient (R^2) or the coefficient of determination is defining the proportion of the total variation that is explained by the regression model. R^2 was equal to 0.74, even though the ideal value of R^2 is 1.0. By considering only terms that have P-value greater than 0.05, the regression model for depth-of-cut is:

$$\begin{aligned} \text{Depth of cut} = & RMS + 0.679 A + 0.221 B + 0.747 C + 0.283 BCD - \\ & 0.555 BC - 0.483 BD - 0.531 CD \end{aligned} \quad (2)$$

Table 3. Results of the regression analysis

Term	Coefficients	Standard Error	P-value
A	0.458027196	0.135298779	<0.001
B	0.310765332	0.178199015	<0.001
C	0.10117213	0.135298779	<0.001
D	0.34229949	0.135298779	<0.001
BCD	0.129621098	0.028992595	0.045915
BC	-0.254232066	0.073989766	0.019516
BD	-0.22136221	0.073989766	0.022184
CD	-0.242919954	0.04595871	0.014893
ABCD	0.006265863	0.009848295	0.526821
ABC	-0.012531727	0.028992595	0.666977
ABD	0.052554416	0.028992595	0.74429
AB	-0.105108833	0.073989766	0.160144
AC	-0.055339244	0.04595871	0.232849
AD	-0.142120768	0.04595871	0.29009

In order to assess the goodness of fit and to the potential redundancy of data, a residual analysis with Quantile-Quantile Plot (Figure 7) and Anderson-Darling test were conducted. The figure shows that the residuals follow a normal distribution without skew neither to left nor right and the residuals scattered about a straight line, also Anderson–Darling test lead to the same conclusion. Anderson–Darling test gave the value of 0.852.

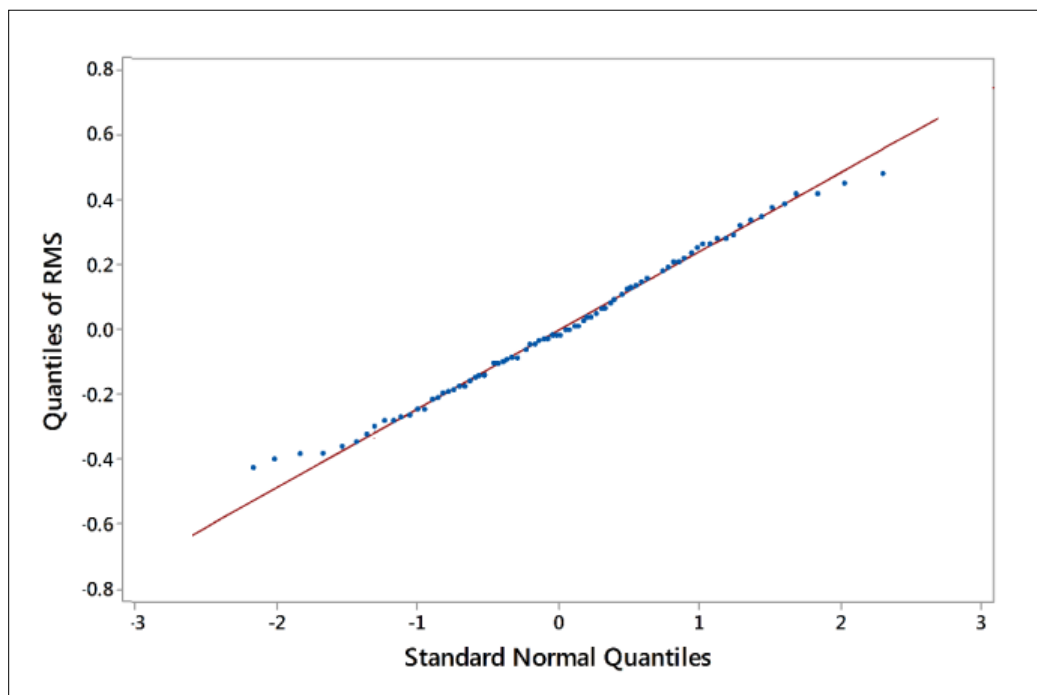


Figure 7. Quantile-quantile plot for RMS residuals

3.3. ARTIFICIAL NEURAL NETWORK BASED MODELING

The artificial neural network is statistical machine learning tool established based on the idea of how neurons in human brain work. The neural network consists of layers and nodes called neurons the number of layers and neurons depends on the difficulty of the problem being modeled. The input and output layers have neurons equal

to the number of the inputs and the outputs respectively. The neurons connected by synapses which take a value from an input neuron and multiply it by specific weight and output the results, neurons have a more complicated purpose, they add together all outputs from all synapses and apply activation function.

A sigmoid function was used to map the output of the hidden layer to the range of values of (0, 1), This function was selected because it is one of the common types of transformation functions and provides a mean of establishing a storing, complex, and nonlinear relationships between the inputs and output data sets as shown in Figure 8.

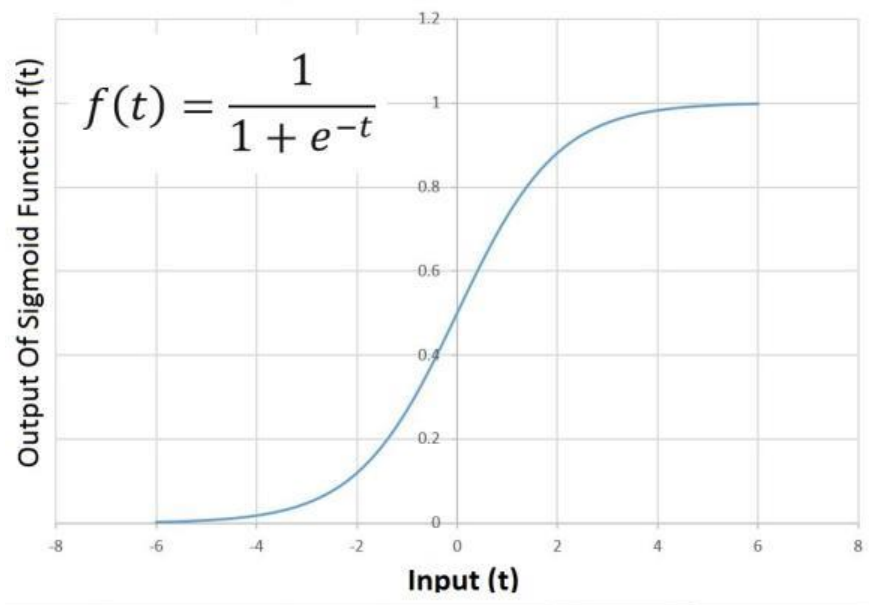


Figure 8. Sigmoid activation function

An artificial neural network at least has three layers; input layer, hidden layer, and output layer. If X is the input data vector which in this work is 1 by 4 vector Figure 9,

$W(1)$ is weight matrix which is 4 by N matrix, where N is the number of neurons in the hidden layer, and $Z(2)$ is the transfer function of the second layer.

$$Z^{(2)} = X \times W^{(1)} \quad (3)$$

By applying transfer function to each element in $Z^{(2)}$, $a^{(2)}$ activation function of the second layer can be obtained by

$$a^{(2)} = f(Z^{(2)}) \quad (4)$$

$a^{(2)}$ has the same size as $Z^{(2)}$. Now by multiplying weight matrix of second layer $W(2)$ which is N by 1 matrix where there is only one output in our artificial neural network which is depth of cut

$$Z^{(3)} = a^{(2)} \times W^{(2)} \quad (5)$$

$Z^{(3)}$ is the transfer function of the third layer. Finally, activation function is applied to $Z^{(3)}$ in order to obtain the estimate for depth of cut y'

$$y' = f(Z^{(3)}) \quad (6)$$

Without training the network the estimation error will be very large, training is the process of updating the weight matrix to minimize the cost function J

$$J = \sum \frac{1}{2} (y - y')^2 \quad (7)$$

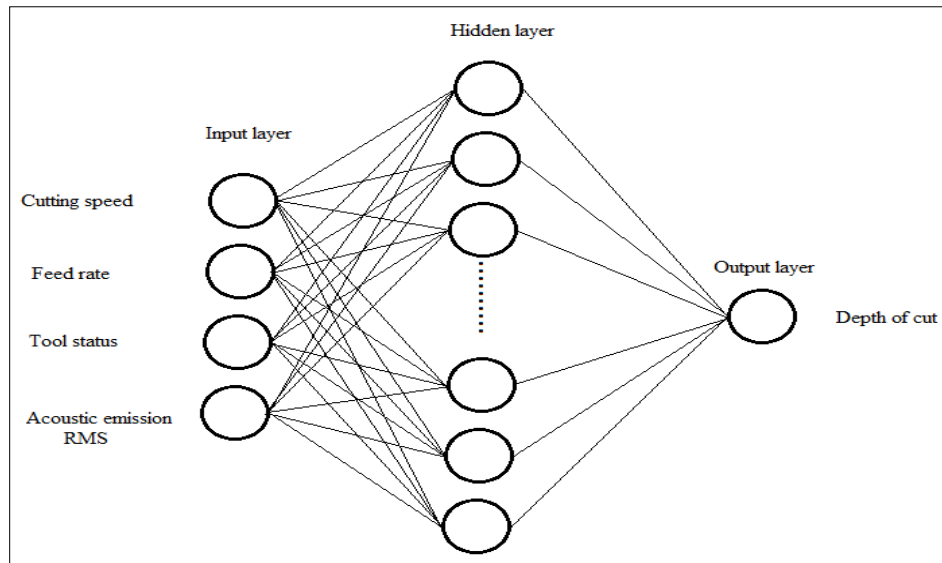


Figure 9. Neural network architecture

One of the training algorithms can be used to train the ANN is a supervised learning algorithm called Backpropagation algorithm which adjusts two parameters learning rate and momentum coefficient and keep them between 0 and 1. Equation 7 can be written as

$$J = \sum \frac{1}{2} (y - f(f(XW^{(1)})W^{(2)}))^2 \quad (8)$$

In order to save time and reduce calculations Gradient Descent method is used to guarantee searching for J in the correct direction and stop searching when smallest J is reached (cost function stops decreasing) by taken the partial derivative of J with respect of W ($\frac{\partial J}{\partial W}$), when $\frac{\partial J}{\partial W}$ is positive then the cost function is increasing and vice versa. This method is useful especially in multidimensional problems. Gradient descent can be performed either after using of all training data (batch gradient descent) or after each input–output pair (sequential gradient descent).

The neural network was trained with 147 data points (cutting conditions) to estimate the weights (includes biases) of candidate designs, and 48 data points were used to estimate the non-training performance error of candidate designs and also used to stop training once the non-training validation error estimate stops decreasing. Also, 48 data points were used as testing data to obtain an unbiased estimate for the predicted error of unseen non-training data. Training, validation, and testing data were randomly chosen from different cutting conditions from the data set consists of 243 data points (cutting conditions).

Figure 10 illustrates the mean square error versus iteration (Epochs) number, while using the Bayesian regularization training algorithm. The correlation coefficient (R^2) or the coefficient of determination indicates that explained proportion of the total variation by the ANN model was equal to 0.86 which better than the result obtained in regression analysis by 16.21 %. For the superior performance of the ANN model, it will be used for the rest of this paper to estimate depth-of-cut for different cases.

4. ESTIMATION OF DEPTH-OF-CUT

Figure 11 shows the depth-of-cut estimated at 2 mm, 1 mm, and 0.5 mm with a feed rate of 40 mm/min and a cutting speed of 5000 rpm. Clearly, the system can detect the depth-of-cut with a maximum acceptable error. The accuracy of depth-of-cut estimation depends on the quality of the acquired signal.

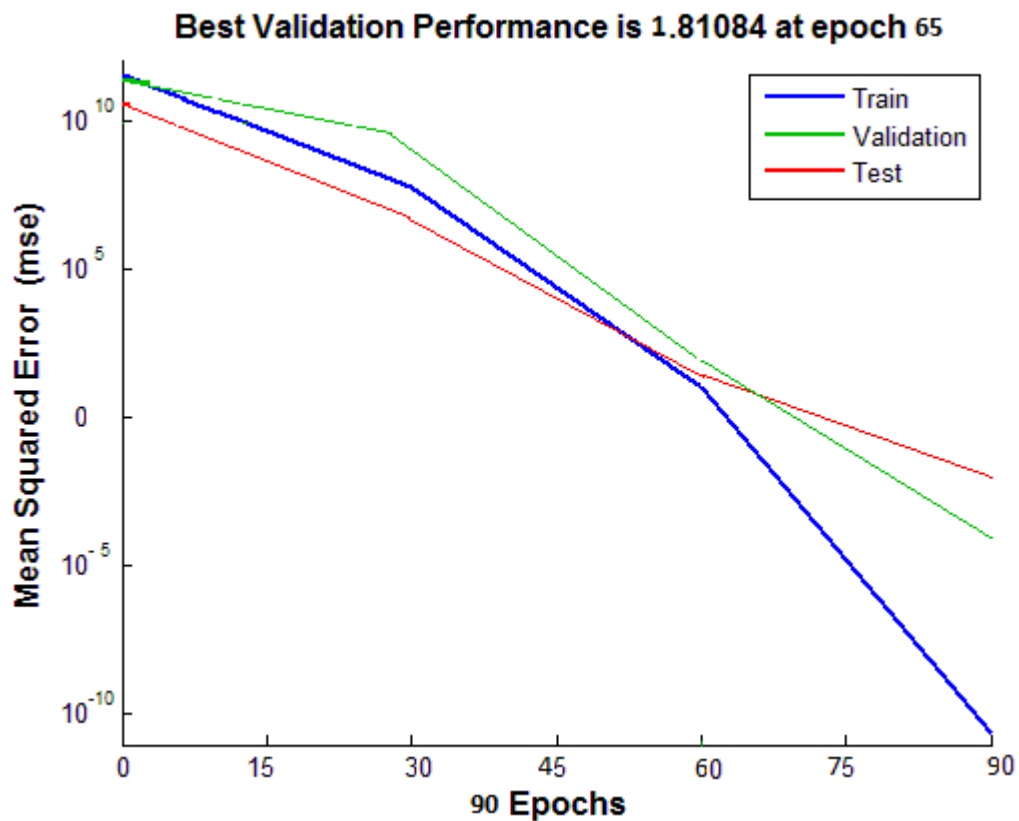


Figure 10. Neural network performance

This work tested the efficiency of the model in estimating depth-of-cut in an interrupted cutting process. As shown in Figure 12, a 25.2 mm slot was made in the workpiece perpendicular to the machining direction. The depth-of-cut was 1 mm, the

cutting speed was 4000 rpm, the feed rate was 30 mm/min, and the tool was fresh. 51 second is the time required for the tool to cross the gap ($25.2/30$), and 25 second is both engagement and disengagement time subtracted from 51 seconds. Figure 10 shows that the model is able to distinguish the slot; thus, the system is capable of detecting the engagement and the disengagement of the tool with the workpiece as well as the depth-of-cut.

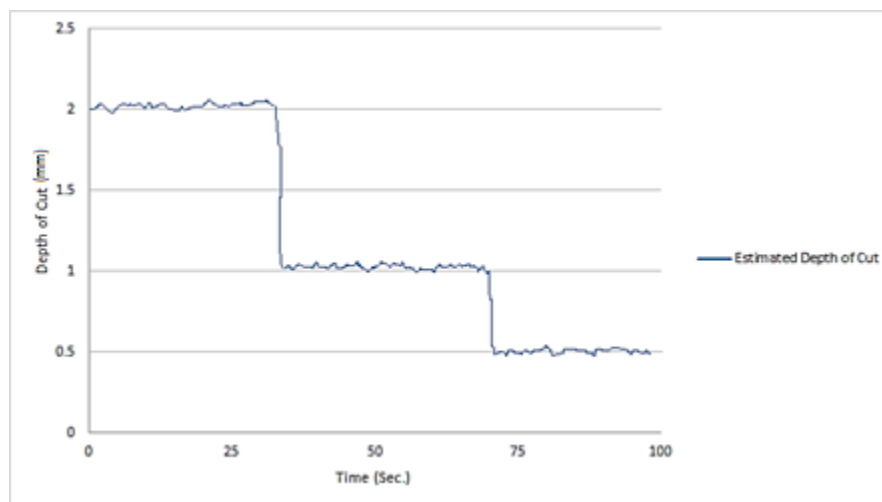


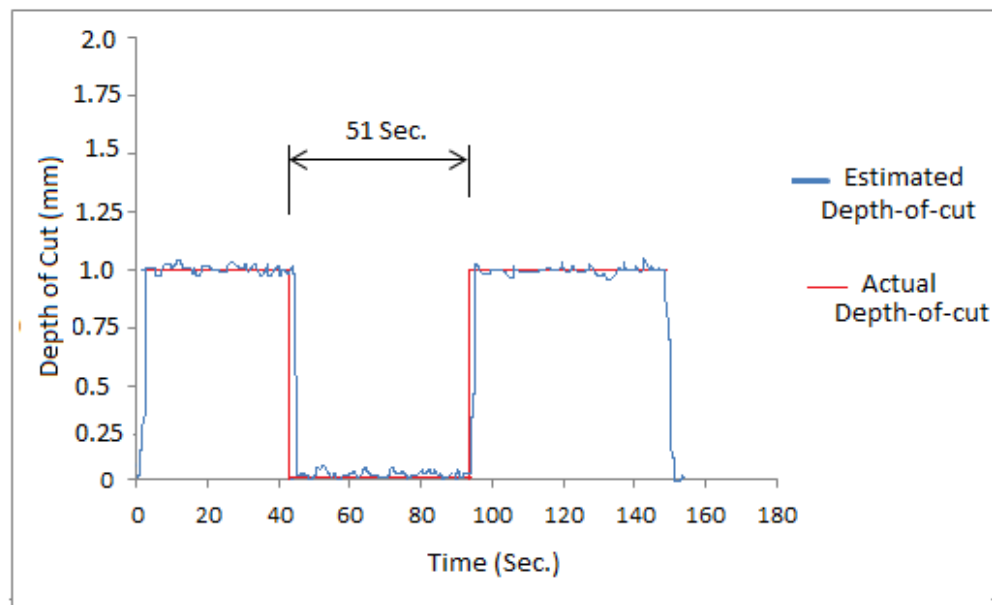
Figure 11. Depth-of-cut estimation

Figure 13 shows both the nominal and estimated depth of cut for inclined surface cutting. A 10 mm ramp was created at the end of 60 mm cutting with 2 mm height as shown in the cutting geometry in the figure. The cutting speed was 4000 rpm, the feed rate was 30 mm/min, and the tool was fresh.

As final test for the efficiency of the depth-of-cut detecting system, a free-form surface was made from stainless steel 316 using laser deposition. The deposited part scanned twice after and before being machined using a Nextengine 3-D scanner Figure

14, it takes about 2 minutes per scan of each surface with the dimensional accuracy of 0.005 inches in macro mode and 0.015 inches in wide mode, then the part was machined and scanned again as shown in the figure.

In this work, a substrate is selected to be the reference plane. Three points were marked on the substrate by laser flash, for the reason that the 3- D scanner can capture points on the surface precisely. These three points make the reference plane and scanner coordinate system on the substrate. One of the three points is the origin (B), the second point (a) and the origin can determine x-axis and z-axis is parallel to the normal of the plane of three points, then y-axis can be determined exclusively by x-axis, and z-axis, as shown in Figure 15. The following steps were used to describe the used setup to measure the surfaces difference



(a)

Figure 12. Interrupted cutting (a) nominal/estimated depth-of-cut (b) cutting geometry

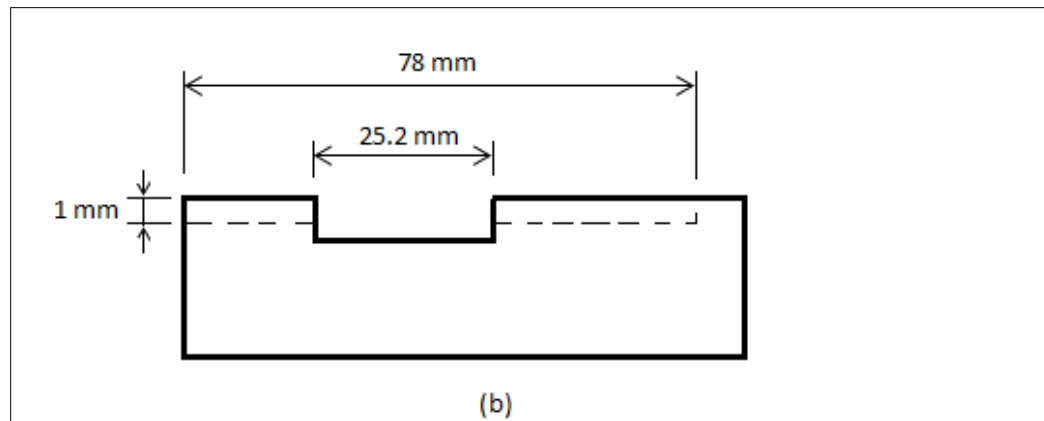


Figure 12. Interrupted cutting (a) nominal/estimated depth-of-cut (b) cutting geometry (Cont.)

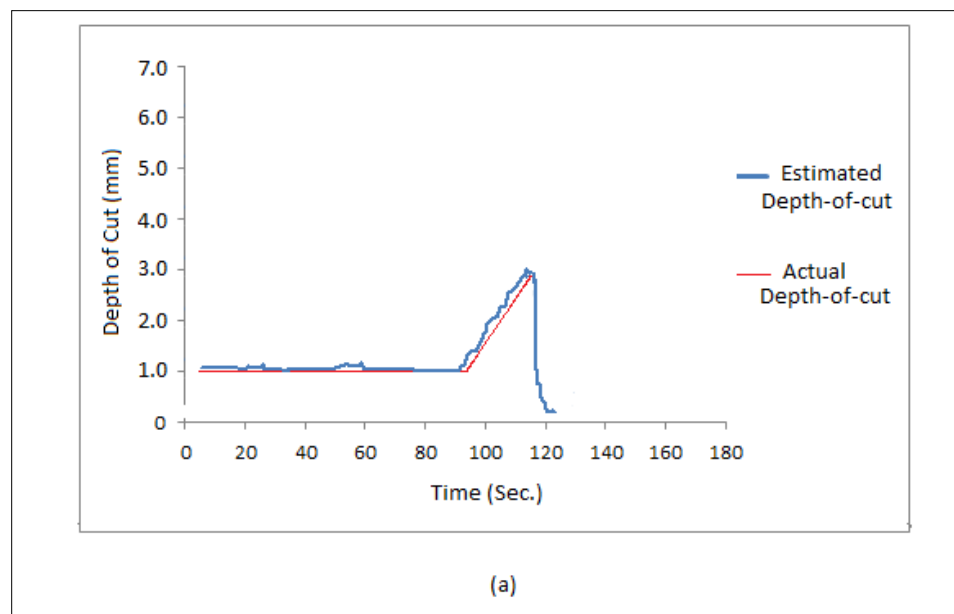


Figure 13. Inclined surface cutting (a) nominal/estimated depth-of-cut (b) cutting geometry

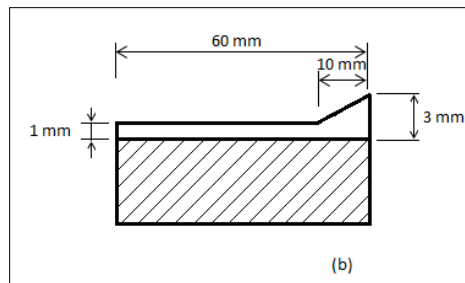


Figure 13. Inclined surface cutting (a) nominal/estimated depth-of-cut (b) cutting geometry (Cont.)

- After constructing the coordinate reference system as described above, a powder metal was deposited on the substrate, then the part was rotated to face the 3-D scanner and the top surface was scanned. Grey paint was used to cover shiny surface



Figure 14. Scanning the part before machining

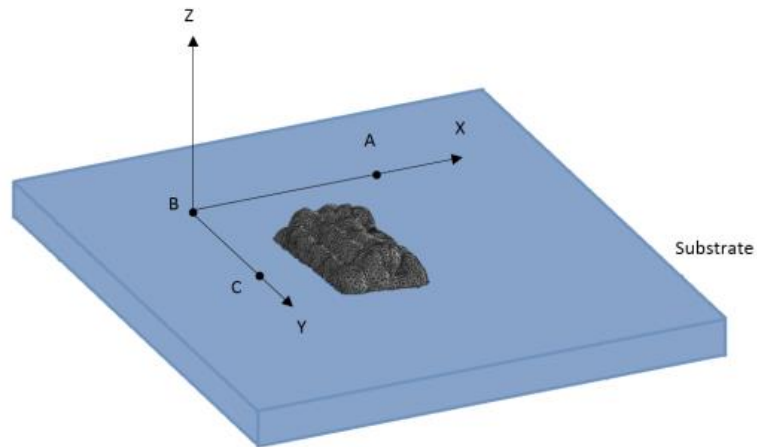


Figure 15. The coordinate reference system using three points

- The part was machined and the acoustic emission signal was recorded, the part was rotated to the same position before machining and scanned once more. This will eliminate the need of removing the part consequently get rid of fixture errors.
- The two scans were saved as Standard Triangulation Language (STL) model, and aligned using the three-point reference coordinate. The accuracy of the coordinates alignment found to be the same as the accuracy of the 3-D scanner, which is 0.005 inch.
- Using a series of parallel planes slicing the models turns the 3-D surface to 2D profiles.

The area created by the 2D profiles is the machined material. The machined material was sliced to fifty sections as shown in Figure 16 and the area of each section was calculated. In order to calculate the depth-of-cut, the area of each section was divided by the tool diameter (12.7 mm).

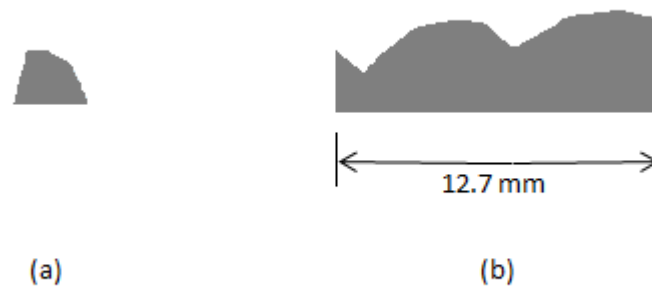


Figure 16. Machined material slicing (a) first section. (b) fifteenth section

Figure 17 shows the measured depth-of-cut from the sections and detected depth-of-cut by the acoustic emission sensor. The feed rate was 60 mm/min, cutting speed 4000 rpm, cutting length about 52 mm and the tool was worn-out. There is some difference between the measured and detected depth-of-cut in several points. This error might be caused by the change in the shear strength of the deposited material where the depth-of-cut detection model was made with material deposited at 800 W laser energy and the material tested now was made at 1000 W laser energy.

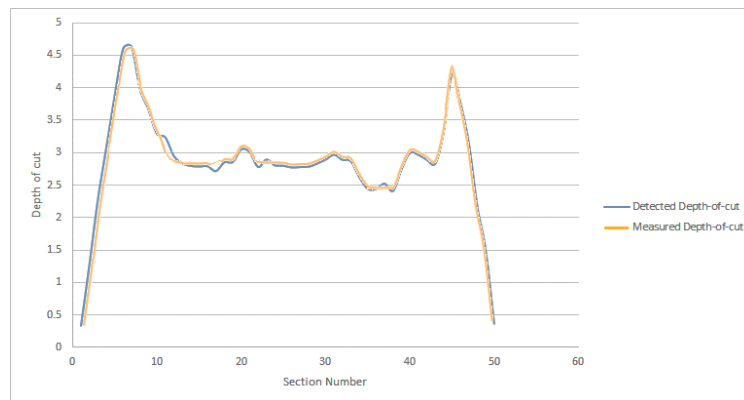


Figure 17. Measured and detected depth-of-cut for a deposited material

5. CONCLUSIONS

This research investigated experimentally the depth-of-cut and the acoustic emission variations during end-milling of deposited stainless steel 316. A full factorial experimental design was used to conduct experiments. Regression analysis results compared to the neural network results, the neural network showed better results in modeling the experimental data. As a result of this work, neural network model was adopted to predict depth-of-cut in end milling.

The Bayesian regularization training algorithm was used to train the network. 25 neurons were used within the hidden layer, the results obtained after training showed the effectiveness of this approach.

The model confirmed the effectiveness of estimating depth-of-cut for during cutting inclined surface. The model is capable to distinguish the slot in an interrupted cutting process; therefore, the system is capable of detecting the engagement and the disengagement of the tool with the workpiece as well as the depth-of-cut.

The main concern of this work was to detect the depth-of-cut for part made with, a free form surface process such as Laser Metal Deposition, the model showed good agreement between measured depth-of-cut by using a 3D scanner and the predicted depth-of-cut by the artificial neural network model.

6. FUTURE WORK

Future work will investigate signal processing and feature extraction since the root mean square is provided by the coupler and there is no control on low-pass and high-pass filters. A raw signal can be acquired from the sensor, and this signal contains more

information than the root mean square signal, which was already processed inside the coupler. Also, the neural network approach can also be used to estimate feed rate, cutting speed or tool wear when the other cutting parameters are given.

The transferability of the prediction model to other systems or machines could be effected by some factors such as part size and geometry, tool diameter, and / or sensor position, a study needs to be conducted to investigate the effect of each factor on the model. Using multi-sensor fusion system could reduce the sensitivity of the model to these factors.

APPENDIX

Table 1. Full factorial design of experiments with average RMS

Experiment	Depth-of-Cut (mm)	Cutting Speed (RPM)	Feed Rate (mm/round)	Tool Status	Average RMS
1	1	1	1	1	0.538072
2	1	1	1	2	0.501514
3	1	1	1	3	0.464955
4	1	1	2	1	0.556071
5	1	1	2	2	0.322992
6	1	1	2	3	0.089914
7	1	1	3	1	0.57407
8	1	1	3	2	0.144471
9	1	1	3	3	0.285127
10	1	2	1	1	0.492133
11	1	2	1	2	0.379451
12	1	2	1	3	0.266769
13	1	2	2	1	0.364489
14	1	2	2	2	0.249053
15	1	2	2	3	0.133617
16	1	2	3	1	0.236845
17	1	2	3	2	0.118655
18	1	2	3	3	0.000465
19	1	3	1	1	0.446195
20	1	3	1	2	0.257389
21	1	3	1	3	0.068583
22	1	3	2	1	0.172907
23	1	3	2	2	0.175114
24	1	3	2	3	0.177321
25	1	3	3	1	0.10038
26	1	3	3	2	0.092839
27	1	3	3	3	0.286058
28	2	1	1	1	0.528589

Table 1. Full factorial design of experiments with average RMS (Cont.)

29	2	1	1	2	0.49203
30	2	1	1	3	0.455472
31	2	1	2	1	0.546588
32	2	1	2	2	0.313509
33	2	1	2	3	0.080431
34	2	1	3	1	0.564587
35	2	1	3	2	0.134988
36	2	1	3	3	0.29461
37	2	2	1	1	0.48265
38	2	2	1	2	0.369968
39	2	2	1	3	0.257286
40	2	2	2	1	0.355006
41	2	2	2	2	0.23957
42	2	2	2	3	0.124134
43	2	2	3	1	0.227362
44	2	2	3	2	0.109172
45	2	2	3	3	0.009018
46	2	3	1	1	0.436711
47	2	3	1	2	0.247906
48	2	3	1	3	0.0591
49	2	3	2	1	0.163424
50	2	3	2	2	0.165631
51	2	3	2	3	0.167838
52	2	3	3	1	0.109863
53	2	3	3	2	0.083356
54	2	3	3	3	0.276575
55	3	1	1	1	0.519106
56	3	1	1	2	0.482547
57	3	1	1	3	0.445989
58	3	1	2	1	0.537105
59	3	1	2	2	0.304026
60	3	1	2	3	0.070948
61	3	1	3	1	0.555104

Table 1. Full factorial design of experiments with average RMS (Cont.)

63	3	1	3	3	0.304094
64	3	2	1	1	0.473167
65	3	2	1	2	0.360485
66	3	2	1	3	0.247803
67	3	2	2	1	0.345523
68	3	2	2	2	0.230087
69	3	2	2	3	0.114651
70	3	2	3	1	0.217879
71	3	2	3	2	0.099689
72	3	2	3	3	0.018501
73	3	3	1	1	0.427228
74	3	3	1	2	0.238423
75	3	3	1	3	0.049617
76	3	3	2	1	0.153941
77	3	3	2	2	0.156148
78	3	3	2	3	0.158354
79	3	3	3	1	0.119346
80	3	3	3	2	0.073873
81	3	3	3	3	0.267092

REFERENCES

- [1] Duro AJ, Padget JA, Bowen CR, Alicia Kim H, Aydin N (2016) Multi-sensor data fusion framework for CNC machining monitoring. *Mechanical Systems and Signal Processing* 66–67:505–520
- [2] Newman S, Nassehi A, Imani-Asrai R, Dhokia V (2012) Energy efficient process planning for CNC machining. *CIRP J Manuf Sci Technol* 5(2):127–136
- [3] Choi JG, Yang MY (1999) In-process prediction of cutting depths in end milling. *Int J Mach Tools Manuf* 39([Inspec] [ISI]):705–721
- [4] Yang L, DeVor R, Kapoor S (2005) Analysis of force shape characteristics and detection of depth-of-cut variations in end milling. *J Manuf Sci Eng* 127:454. doi:10.1115/1.1947207

- [5] Wan M, Zhang WH (2006) Efficient algorithms for calculations of static form errors in peripheral milling. *J Mater Process Technol* 171:156–165
- [6] Li H, Shin YC (2006) A time-domain dynamic model for chatter prediction of cylindrical plunge grinding processes. *ASME J Manuf Sci Eng.* (in press)
- [7] Kang Y, Wang Z, Wu J, Jiang C (2006) Numerical prediction of static form errors in the end milling of thin-walled workpiece. *IET Conf Pub.* 816, doi: 10.1049/cp:20060872
- [8] Prickett P, Siddiqui R, Grosvenor R (2010) The development of an end-milling process depth of cut monitoring system. *Int J Adv Manuf Tech.* doi: 10.1007/s00170-010-2711-6
- [9] ASTM Standard E610–82 (1982) Standard definitions of terms relating to acoustic emission. American Society for the Testing Materials, West Conshohocken, PA
- [10] Kaiser J (1950) Untersuchungen über das Auftreten Geräuschen beim Zugversuch (An investigation into the occurrence of noises in tensile tests). PhD dissertation. Technische Hochschule, Munich, Germany
- [11] http://faculty.ksu.edu.sa/hossainy/Book2/9159X_05.pdf. Manufacturing Systems, 2000 (March 3, 2011)
- [12] Micheletti GF, Koenig W, Victor HR (1976) In-process tool wear sensors for cutting operations. *Annals of the CIRP* 25:483–488
- [13] Ravindra H, Srinivasa Y, Krishnamurthy R (1997) Acoustic emission for tool condition monitoring in metal cutting. *Wear* 212(1): 78–84
- [14] Chen X, Beizhi L (2007) Acoustic emission method for tool condition monitoring based on wavelet analysis. *Int J Adv Manuf Technol* 33:968–976
- [15] Li X, Yuan Z (1998) Tool wear monitoring with wavelet packet transform—fuzzy clustering method. *Wear* 219(2):145–154
- [16] Zhiqiang M, Guanghui S, Di L, Xing X (2016) Dissipativity analysis for discrete-time fuzzy neural networks with leakage and timevarying delays. *Neurocomputing* 175(Part A):579–584
- [17] Liao Z, Axinte DA (2016) On monitoring chip formation, penetration depth and cutting malfunctions in bone micro-drilling via acoustic emission. *J Mater Process Technol* 229:82–93

- [18] Han X, Tianyu W (2013) Analysis of acoustic emission in precision and high-efficiency grinding technology. *Int J Adv Manuf Tech* 67: 9–2, Pages 1997–2006
- [19] ISO 8688–2 (1989) Tool life testing in milling—part 2: end milling, 1st edn. International Organization for Standardization, Geneva, Switzerland
- [20] Goebel K, Yan W (2000) Feature selection for tool wear diagnosis using soft computing techniques. *The ASME International Mechanical Engineering Congress and Exhibition, Orlando*, pp 5– 10
- [21] Sahai H, Ageel MI (2000) *The analysis of variance: fixed, random and mixed models*. Birkhauser, Boston, pp 57–71

II. DEFECTS MONITORING OF LASER METAL DEPOSITION USING ACOUSTIC EMISSION SENSOR

Haythem Gaja ^{* a}, Frank Liou ^a

^aMissouri University of Science and Technology, Mechanical & Aerospace Engineering,
400 W 13th Street, Rolla, MO 65409-0050, USA

ABSTRACT

Laser metal deposition (LMD) is an advanced additive manufacturing (AM) process used to build or repair metal parts layer by layer for a range of different applications. Any presence of deposition defects in the part produced causes change in the mechanical properties and might cause failure to the part. Corrective remedies to fix these defects will increase the machining time and costs. In this work, defects monitoring system was proposed to detect and classify defects in real time using an acoustic emission (AE) sensor and an unsupervised pattern recognition analysis (K-means clustering) as well as a principal component analysis (PCA). The characteristics of the AE signal obtained in LMD processes can be complex in terms of both nonlinearities, and nonstationary. To overcome this complexity, time domain and frequency domain, and relevant descriptors were used in the classification process to improve the characterization and the discrimination of the defects sources. The methodology was found to be efficient in distinguishing two types of signals that represent two kinds of defects which are cracks and porosities. A cluster analysis of AE data is achieved and the resulting clusters correlated with the defects sources during laser metal deposition.

Keywords: Laser metal deposition - Deposition defects - Acoustic emission – Clustering analysis - Principal component analysis

1. INTRODUCTION

In general additive manufacturing is extensively used even though monitoring and detection of defects during AM still require a better understanding. One of the difficulties in using an adaptive control and LMD monitoring system is the accurate detection of defects as being formed during the metal deposition. The purpose of monitoring laser metal deposition process is to prevent and detect damage of produced part for any deposition path and part design. In the LMD process, particular changes in the acoustic emission signal indicate the present of defects, these changes must be carefully considered to ensure the effectiveness of the control system. AE has the advantage of real-time, continuous monitoring of LMD. The central goal of such a system is to indicate the occurrence of defects events, but classifying the type of defect is also necessary for the better use of the system and suggestion of corrective remedies.

Laser metal deposition (LMD) is one of powder-based laser deposition additive manufacturing techniques such as laser cladding (LC) [2,3], laser direct casting (LDC) [4,5], direct metal deposition (DLD) [6], directed light fabrication (DLF) [7,8,9], laser forming (Lasform) [10], shape deposition manufacturing (SDM) [11], laser engineered net shaping (LENS) [12,13], free form laser consolidation (LC) [14,15], and many others. The main process parameters of LMD; laser power, travel velocity, and powder flow rate control the geometry accuracy and the mechanical properties of the finished part by determining the size of the molten pool, the part deformation, and the microstructure of

the deposited layers. They affect the temperature profile and cooling rate in the molten pool, as well as the thermal cycles at each location of the fabricated part [1].

The acoustic emission sensor is a piezoelectric transducer generates an electrical charge as a response to the elastic waves emitted from sources inside a material as a result of the sudden release of energy. The AE technique is one of most powerful monitoring technologies; it has been used for monitoring in many manufacturing processes such as the cutting operations [16,17,18] and the welding processes. Jolly [1] monitored the crack growth in stainless steel welds. It was found that a maximum AE rate is directly related to the number of cracks in the weld defect zone. This work is considered to be the first most significant milestone in the application of the AE technique for monitoring the welding process [2]. A.S.Sun. Rostek [3] in 1990 used computer-aided acoustic pattern recognition to demonstrate the monitoring capabilities of acoustic signals. Duley and Mao. [4] studied the laser welding process of aluminum 1100 using acoustic emission. They found that a keyhole could be identified by the AE frequency components and correlated the AE with laser penetration and surface condition. Grad et al. [5] in 1996 developed a monitoring method using different statistical parameters to assess process stability.

Bohemen [6] demonstrated that martensite formation during gas tungsten arc (GTA) welding of steel 42CrMo4 can be monitored by means of AE. It was shown that a particular relation exists between the root mean square (RMS) value of the measured AE and the volume rate of the martensite formation during GTA welding. Recently, Grad et al. [7] examined the acoustic waves generated during the short circuit gas metal arc

welding process. It was found that the acoustic method can be used to assess welding process stability and to detect the severe discrepancies in arc behavior.

Yang [9] recently used an Acoustic emission (AE) sensor to identify damage detection in metallic materials. Results suggested a strong correlation between AE features, i.e., RMS value of the reconstructed acoustic emission signal, and surface burn, residual stress value, as well as hardness of steels. Diego-Vallejo [8] in his work found that the focus position, as an important parameter in the laser material interactions, changes the dynamics and geometric profile of the machined surface and also the statistical properties of measured AE signal.

However, more research needs to be done regarding using the acoustic emission sensor in monitoring laser metal deposition. In this paper, the defects type distinguishing of the LMD and its corresponding key features are investigated by clustering the AE signals. The acoustic emission (AE) technique is suitable to examine the defects sources during LMD because of containing rich defect-related information such as crack and pore formation, nucleation and propagation. Information on defects development is difficult to obtain by only using the AE waveform in a time-space, as a non-stationary process, thus other features such as amplitude, energy, rise time, count and frequency are extracted to analyze qualitatively defects mechanisms.

The purpose of the present work is, first to detect laser metal deposition defects as formed layer-by-layer to take the necessary correction action such as machining and remitting, second to develop a reliable method of analysis of AE data during LMD when several AE sources activated to categorize the defects into clusters based on the defect type.

2. EXPERIMENTS AND DATA COLLECTION

Figure 1 shows a schematic diagram of the experimental set-up. The YAG laser was attached to a 5-Axis vertical computer numerical control machine that is used for post-process machining after LMD. Picoscope 2205A works as a dual-channel oscilloscope to capture the AE signal and stream it to a computer for further analysis, the oscilloscope measures the change in the acoustic emission signal over time, and helps in displaying the signal as a waveform in a graph. An acoustic emission sensor (Kistler 8152B211) captured a high-frequency signal. The bandwidth of the AE sensor was 100 kHz to 1000 kHz. The raw signals were first fed through the data acquisition system and then processed and recorded using the Matlab software.

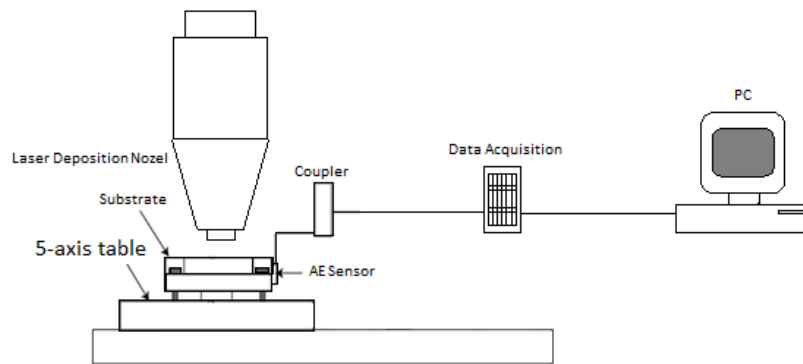
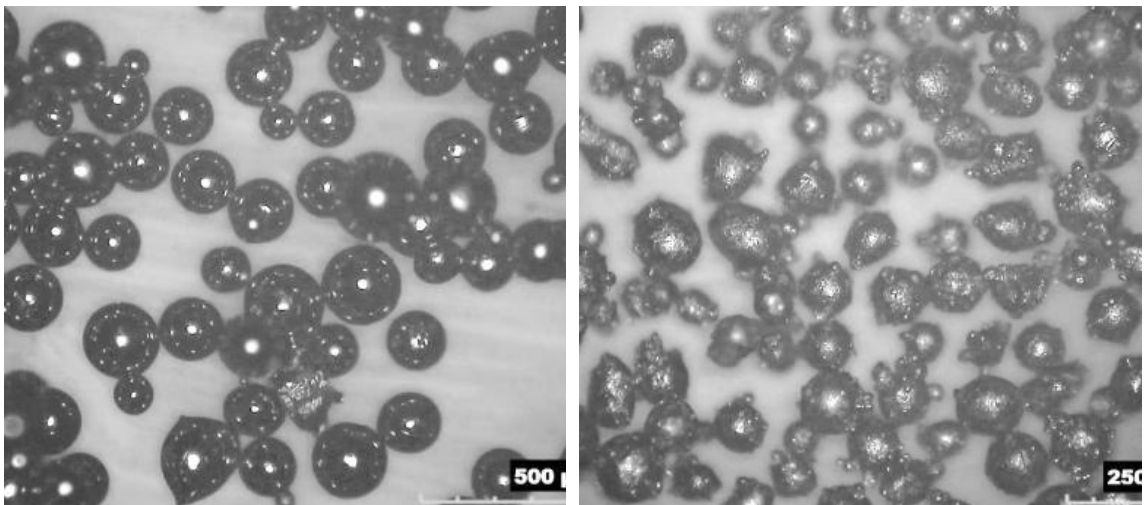


Figure 1. Experimental setup shown the LMD system and AE data acquisition system

A powder feeder system is used to deliver the atomized powder to melt pool by means of argon gas, argon gas is also used as a shielding gas; it flows through channels in the nozzle of laser deposition head to reduce oxidation of the deposit. During laser metal deposition process, porosities and cracks can be formed as the result of lack of fusion,

shield gas trapping, and the difference in thermal coefficients of the deposited material and the substrate. The acoustic emission signal was recorded during a laser deposition process in an oxidized environment and contaminated powder to induce pores and cracks as a result of thermal coefficient difference. The material of the substrate was tool steel. Cracks and porosities were simulated by mixing the mainly Ti-6Al-4V powder with H13 tool steel powder. Table 1 shows the chemical composition and the thermal properties of both powders. The two powders particles as illustrated in Figure 2 are non-uniform in shape and size and may contain internal voids which can cause deposition defects when they mixed. Table 1 displays the chemical composition and the thermal properties of both powders.



(a) Ti-6Al-4V Metal Powder

(b) H13 Metal Powder

Figure 2. Optical image of the metal powders used in deposition process

Table 1. The composition and thermal properties of titanium and tool steel metallic powders (mass %)

	Ti-6Al-4V	H13
Iron, Fe	< 0.25	Balance
Chromium, Cr	-	4.75 – 5.5
Molybdenum, Mo	-	1.1 – 1.75
Silicon, Si	-	0.80-1.20
Vanadium, V	3.50 to 4.50	0.80-1.20
Carbon, C	< 0.08	0.32-0.45
Nickel, Ni	-	0.3
Manganese, Mn	-	0.20-0.50
Titanium, Ti	Balance	-
Aluminum, Al	5.50 to 6.50	-
Thermal expansion ($^{\circ}\text{K}^{-1}$)	11×10^{-6} - 15×10^{-6}	13×10^{-6} - 16×10^{-6}
Thermal conductivity (W/mK)	8	28.6

Figure 3 illustrates the main steps in the developed procedure which used to analyze the AE data. A layer is created by injecting the metal powder into a laser beam which is used to melt the surface of a substrate and create a small molten pool and generate a deposit. The AE sensor is attached to a substrate to transform the energy released by the laser deposition into acoustic emission signal. The total length of the deposition is 15 mm was performed with standard parameters for depositing titanium powder as shown in Table 2.

The formation of porosities and cracks leads to generate an acoustic emission signal; an elastic wave that travels from the source toward a sensor, moving through the substrate until it arrives at the acoustic emission sensor. In response, the sensor produces an electrical signal, which is passed to electronic equipment for further processing and detection of a defect. Since the LMD is an additive process and it deposits metals layer by layer, the AE signal was recorded for each layer and analyzed to extract any useful information from the AE events.

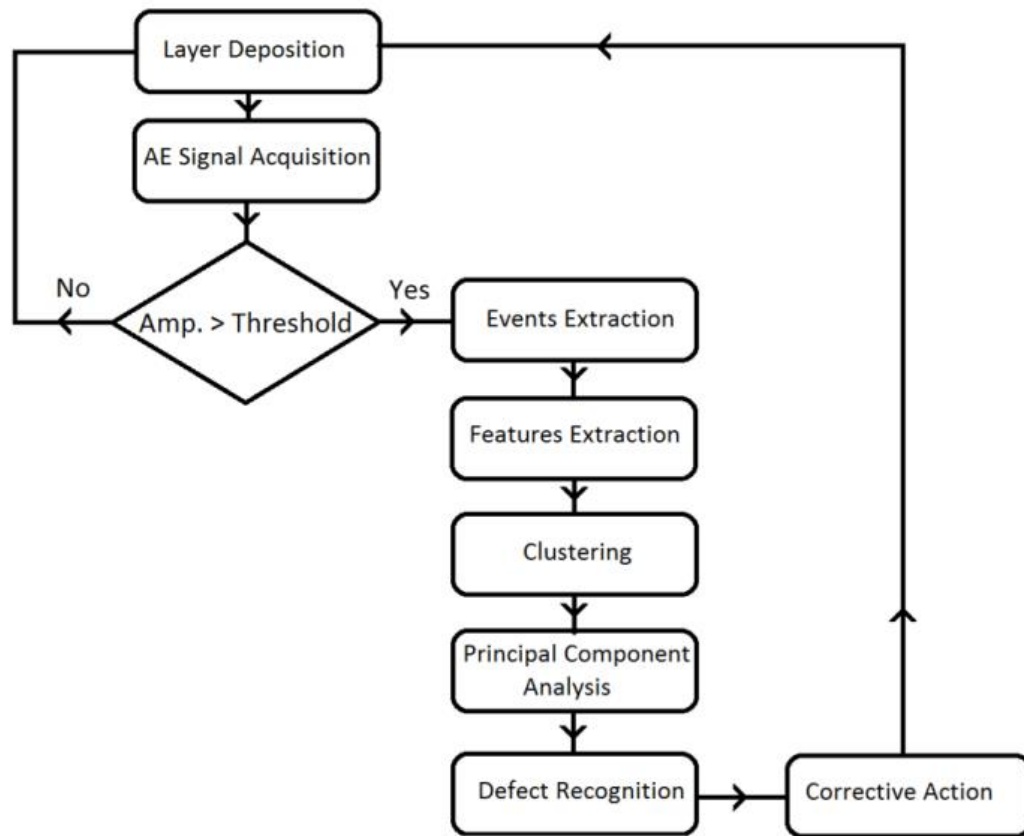


Figure 3. Step-by-step operations used to perform the acoustic emission analyses

Table 2. Laser metal deposition process parameters

Parameter	Value
Laser power	1,000 Watt
Powder feed rate	10 g/min
Table velocity	300 mm/min
Length of track	15 mm
Layer thickness	About 0.5 mm
Layer width	About 2.5 mm

Figure 4 shows an AE signal acquired during LMD process in the presence of defects, the spikes in the signal are events which have features different from the rest of the AE signal. The AE event is counted when the amplitude of the signal is higher than a preset threshold which is the background noise preceded and followed by a signal with amplitude lower than the threshold for a certain period.

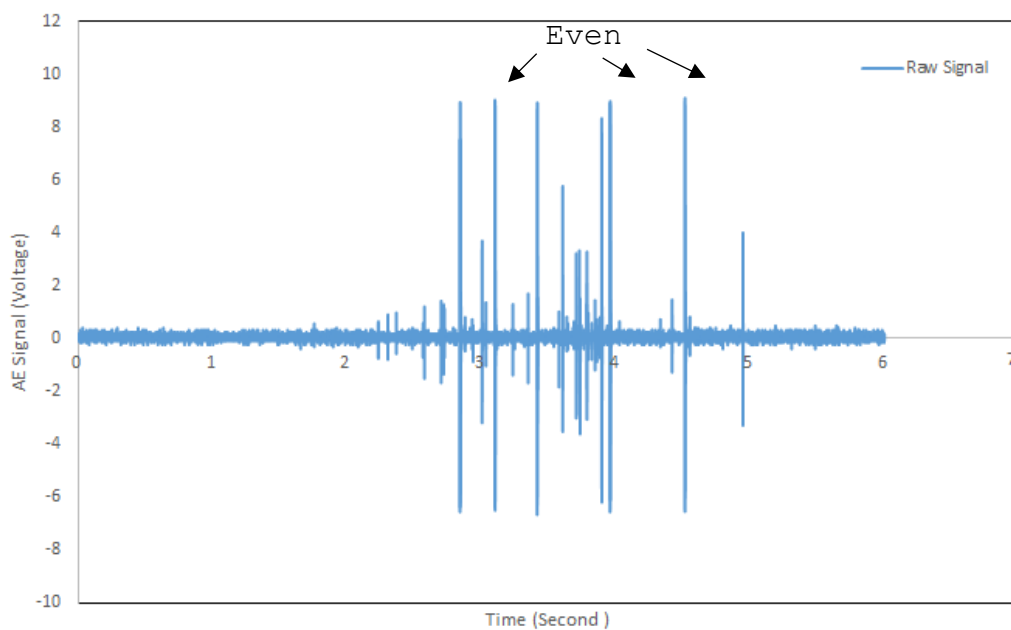


Figure 4. AE raw signal acquired during LMD process

Different defect mechanisms can produce similar waveform and amplitude; it is not sufficient to use a particular feature to represent the events. Therefore, seven AE signal features (Table 3) were employed in the clustering analysis to overcome this problem. Representing the AE signal with enough features is critical to collect as much information as possible about the emitting source, especially there is little literature

regarding using AE technique in motoring LMD process that can be used as a reference in AE features selection. The AE signal can be represented in the frequency domain using Fast Fourier Transform (FFT) or in the time domain using peak amplitude, kurtosis, energy, the number of counts, duration, and rise time. Figure 5 shows some of the time-dependent features.

Table 3. Time domain and frequency domain AE signal features

Feature	Definition
Peak Amplitude	It is the greatest measured voltage in an AE event
kurtosis	<p>It is a measure of whether the data of an AE event are peaked or flat compared to a normal distribution.</p> $\text{Kurtosis} = \frac{\sum_{i=1}^N (x_i - \bar{x})^2 / N}{\sigma^4} - 3 \quad (1)$ <p>Where N is the number of samples (x_i) in an AE signal, σ is the standard deviation, and \bar{x} is the mean.</p>
Energy	<p>Since the domain of the AE event signal is discrete, the energy of the signal is given by</p> $\text{Energy} = \sum_{i=1}^N (x_i)^2 \quad (2)$
Number of Counts	It is the number of pulses emitted by the AE event.
Duration	It is the time difference between the first and last threshold crossings.
Rise Time	It is the time interval between the first threshold crossing and the AE event peak.
Peak Amplitude Frequency	It is a characterization of the magnitude and frequency of an AE event using Fast Fourier transform

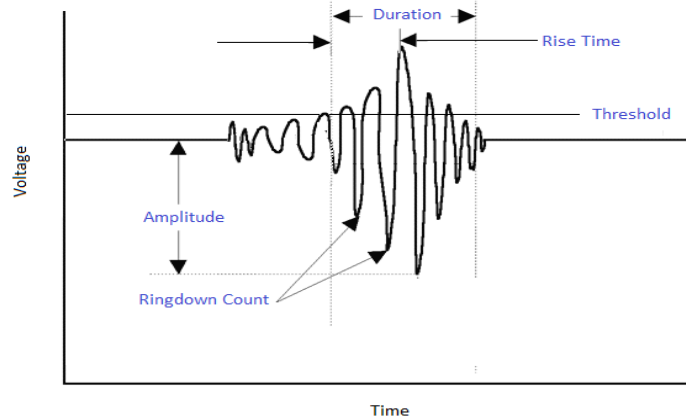


Figure 5. Time dependent AE event features

Among all the features, the signal amplitude alone was measured in real time by the data acquisition system. All the other descriptors were calculated from the waveforms at the end of the deposited layer because they are very dependent on the amplitude threshold used to detect the arrival time and the end of an AE signal. In this work, all these features were used in multi-parameter statistical analysis and clustering analysis. No AE noise associated with the operation of the laser system or the CNC system were observed. Also, it was found in this study the noise level is much smaller than the signals of interest. Also, a frequency filtering was used which allowing of passing only those signals falling within a selected bandwidth (100 kHz to 1 MHz).

3. RESULTS AND DISCUSSION

3.1 PRINCIPAL COMPONENT ANALYSIS

Principal component analysis (PCA) was used here for the sake of dimensionality reduction, the results of the clustering analysis cannot be visualized in their original

dimension (seven-dimensional data set). PCA is a statistical technique which utilizes an orthogonal transformation to convert a set of correlated variables into a set of values linearly uncorrelated known as principal components. PCA is used to approximate the data matrix of features to reduce the number of related dimensions. This can be done by finding the directions that explain the maximum variation in the dataset, and then project into a subspace with lower dimensions. The seven features calculated from AE events are the components of the n input pattern vectors Z_i ($i = 1, 2, \dots, n$).

$$Z = \begin{bmatrix} z_1^t \\ z_2^t \\ \vdots \\ z_n^t \end{bmatrix} = \begin{bmatrix} z_1^1 & z_1^2 & \dots & z_1^m \\ z_2^1 & z_2^2 & \dots & z_2^m \\ \vdots & \vdots & \ddots & \vdots \\ z_n^1 & z_n^2 & \dots & z_n^m \end{bmatrix} \quad (3)$$

Where n number of events and m number of features. The data are first standardized by subtracting the mean from the dataset for each column then dividing by the column standard deviation (the mean is equal to zero, and the standard deviation is equal to one); Table 4 shows the standardized of the AE signal features. then covariance matrix can be calculated by

$$Cov_Z = E[ZZ^T] \quad (4)$$

Z^T is the transpose matrix of matrix Z . Computing eigenvectors and corresponding eigenvalues

Table 4. Standardized of the AE signal features

Event Number	Rise Time	Peak amplitude	Duration	Kurtosis
1	-0.8632828	-0.7341107	-0.68626	-1.44472
2	-0.1261721	-0.6508765	-0.60598	-1.25783
3	-0.6931803	-0.6231318	-0.62959	-0.34811
4	-0.0694712	-0.5398975	-0.51153	-0.52405
5	-0.2584740	-0.4844081	-0.55876	0.728254
6	-0.2962745	-0.5121528	-0.28959	-0.16773
7	-0.5797787	-0.5676423	-0.53514	0.00428
8	2.803370	2.0958524	2.3407	-1.1222
9	-0.1072718	-0.6786212	-0.53987	-0.14773
10	-0.5608784	-0.7063660	-0.64376	-1.04886
11	-0.3151748	0.3201892	-0.02042	0.449555
12	-0.3340751	-0.4844081	-0.68626	1.881232
13	2.1796615	2.0958524	1.953476	-0.93525
14	-0.1828729	-0.5121528	-0.29903	0.510621
15	-0.5041776	-0.3734291	-0.33681	0.103122
16	1.8583568	2.0958524	1.967643	-1.38266
17	-0.1639726	-0.6231318	-0.23292	0.998504
18	0.0628306	0.9860629	0.267636	2.358211
19	-0.8632828	-0.6786212	-0.74765	0.445735
20	-0.7309809	-0.734110	-0.7382	-0.56879
21	-0.5986790	0.1259761	-0.17625	0.437646
22	-0.1828729	0.1814655	0.02208	0.054488
23	-0.5797787	-0.4566633	-0.1007	1.929897
24	-0.5608784	-0.234705	-0.28487	-0.16722
25	-0.0316707	0.1814655	-0.09598	1.216332
26	-0.4852773	-0.6231318	-0.28487	-0.57514
27	-0.2017732	-0.4566633	-0.41237	1.534873
28	-0.4852773	-0.7063660	-0.51626	-0.96409
29	0.0817309	-0.6786212	-0.42653	-1.13012
30	0.8755425	1.9293840	0.65486	1.466014
31	2.7277695	2.0958524	2.760979	-1.11484
32	-0.6931803	-0.734110	-0.69098	0.127625
33	-0.6931803	-0.7063660	-0.72403	0.144849
34	-0.5608784	-0.4566633	-0.23764	-0.33667
35	2.066259	2.0958524	2.765701	-1.07521
36	-0.8632828	-0.6786212	-0.67209	-0.25692
37	-0.0694712	0.4311682	-0.04875	0.176898

Table 4. Standardized of the AE signal features (Cont.)

Event Number	Number of counts	Energy	Frequency
1	-0.75435274	-0.42589	-1.27045
2	-0.6648721	-0.42121	-0.28512
3	-0.6786384	-0.42337	-0.16714
4	-0.5478591	-0.41726	-0.57824
5	-0.5960409	-0.4176	1.576003
6	-0.2174693	-0.41689	0.226959
7	-0.5547422	-0.42265	0.843153
8	2.2535706	2.41352	0.053381
9	-0.5409760	-0.42517	1.349834
10	-0.6924046	-0.42553	-0.08978
11	-0.0109757	-0.31195	1.354937
12	-0.7612358	-0.42228	-0.71316
13	1.9231809	1.795566	-0.14501
14	-0.2381187	-0.41256	0.799576
15	-0.3138330	-0.40788	-0.4526
16	1.7029210	2.668412	-0.04808
17	-0.1142225	-0.42121	1.881284
18	0.3882451	-0.26322	0.568001
19	-0.8438333	-0.42517	-0.77585
20	-0.8300670	-0.42589	-0.82462
21	-0.1555213	-0.35378	-0.48302
22	0.0785047	-0.33756	-0.34344
23	-0.0109757	-0.38877	0.603812
24	-0.2587681	-0.39165	1.376322
25	-0.0316251	-0.36316	-0.00579
26	-0.1761706	-0.42337	-0.00107
27	-0.3620149	-0.4212	-2.1943
28	-0.5203266	-0.42445	-2.15717
29	-0.3757811	-0.42517	1.515988
30	0.8218817	0.066326	-0.03145
31	2.8042202	2.811349	-2.23613
32	-0.7612358	-0.42589	0.776849
33	-0.8094177	-0.42553	0.102579
34	-0.1899369	-0.40212	0.40919
35	2.7835709	2.630087	-0.15449
36	-0.7337033	-0.42517	0.082367
37	-0.0109757	-0.2917	-0.56332

$$Cov_Z \alpha = \beta \alpha \quad (5)$$

where α is the eigenvectors, and β is the eigenvalue for each principal component see Table 2.

As the covariance matrix is a symmetric matrix and an orthogonal basis. The data can be represented in terms of only a few basis vectors of the orthogonal basis in which the data set has the most significant amounts of variance (Table 5).

As can be seen in Figure 6 and Table 5, the first two principal components are explaining 85.7% of the variance, these principal components will be used to reduce the dimension of the set of features from seven dimensions to just two dimensions for better visualization.

Choosing k eigenvectors with the largest eigenvalues to construct eigenvector matrix Y_T . In the last step, transform the data into the new subspace via the equation

$$W = Z Y_T \quad (6)$$

Table 5. Eigenvalues of the seven AE signal features

Eigenvalue	Proportion	Cumulative
4.9119	0.702	0.702
1.0895	0.156	0.857
0.8222	0.117	0.975
0.0826	0.012	0.987
0.0559	0.008	0.995
0.0377	0.005	1
0.0002	0	1

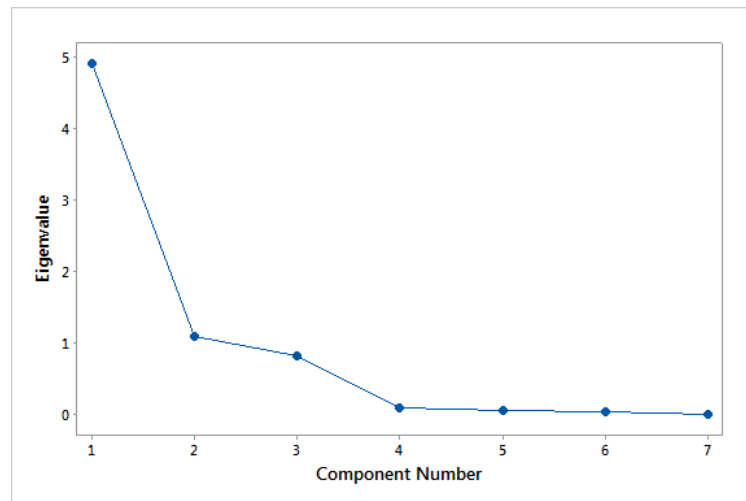


Figure 6. Time-dependent AE event features

which represents the new coordinates of the n patterns in the orthogonal coordinate system defined by the eigenvectors. The reduced dimension will not be used in the clustering analysis to obtain the most accurate clustering results.

3.2. CLUSTERING ANALYSIS

It's not easy to discriminate precisely the AE signal associated with each defect source from the waveform of the signal; thus, it is useful to use clustering analysis. Clustering analysis is a machine learning technique which group the AE events based on their features to create clusters in such a way that the AE events inside a cluster are similar to each other, and also dissimilar from events in other clusters. In this work, the K-means clustering algorithm was used to group the AE events into homogeneous subgroups (clusters). A silhouette width value was used to find the optimal number of clusters.

The K-means clustering algorithm aims to minimize within-cluster distances between all the vectors of a cluster and its center and maximize the distances between the centers of all clusters. The clustering algorithm requires the number of clusters k to be known and specified in advance; thus, the silhouette width was used for a range of clusters from two clusters to ten clusters. The number of clusters with the maximum average silhouette width was used to group the AE events into sub-groups reflecting the number of defects. The k-means algorithm can then be described as follows:

1. Specify the maximum number of clusters (r).
2. Assume the number of clusters k from 1 to r and randomly initialize each cluster center C_i , where i is from 1 to k
3. Calculate the Euclidean distance between the vector and the centers of the clusters and then assign each input vector (or pattern) to the nearest cluster.
3. Recalculate the location of the cluster center according to the nearest mean.
4. Repeat steps 2 and 3 until there are no changes in these center locations.
5. calculate the maximum average silhouette width.
6. Repeat steps from 2 to 5 for all possible number of clusters.

The greater the silhouette value, the better the clustering results [19, 20]. The optimal value of k is determined according to the maximum of the silhouette width defined as

$$s(k) = \frac{1}{n} \sum_{l=1}^n \frac{\min(b(l,k) - a(l))}{\max(a(l), \min(b(l,k)))} \quad (7)$$

where $a(l)$ is the average distance between l -th event and all other events in the same cluster, and $b(l, k)$ is the minimum of the average distances between the l -th event and all the event in each other cluster. The silhouette width values range from -1 to 1. If the silhouette width value for an event is about zero, it means that that the event could be assigned to another cluster. If the silhouette width value is close to -1, it means that the event is well clustered. A clustering can be evaluated by the average silhouette width $s(k)$ of individual events.

The largest average silhouette width, over different K , indicates the best number of clusters. As can be seen, in Table 6 the greatest average silhouette width is 0.8727 which means $k=2$ is the optimum number of clusters. Figure 7 shows the silhouette width values for the individual AE events in clusters one and two; most of the silhouette width values are close to 1 with means that the AE events are well clustered.

Table 6. Average silhouette width for different number of clusters

Number of clusters	Average Silhouette Width
2	0.8727
3	0.4201
4	0.4957
5	0.4902
6	0.4641
7	0.4949
8	0.4416
9	0.4163
10	0.4294
11	0.4117

Table 7 shows the final clusters centers; the final cluster centers are calculated as the mean for each feature within each final cluster, the final cluster centers reveal the characteristics of each detected defect. The defects which represented by cluster two tend to have more energy, longer duration, slower rise time, large number of counts, higher

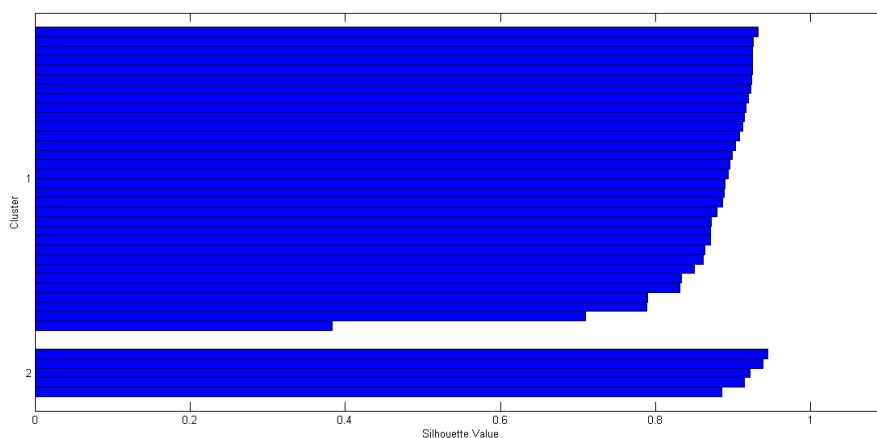


Figure 7. Silhouette width value for the events in the two clusters

amplitude, close to the normal distribution with flatter and light tail distribution, and less frequency compared to the defects which represented by cluster one. Table 7 shows the cluster membership and the distance between each AE event and the center of the cluster, the size of cluster one is 32 which means 86.5 of the AE events; cluster two contains 5 AE events (15.5% of the AE events).

Even though the principal component analysis showed that two principal components are explaining 85.7% of the variance, the third principal component was used for the better representation of the AE events, distribution of the AE events between the two clusters can be seen in Figure 8.

Table 7. Cluster centers

Feature	Cluster	
	1	2
Rise Time (ms)	0.4513268	2.080529
Peak amplitude (volt)	1.8124335	8.8001
Duration (ms)	1.636167	8.2521209
Kurtosis	6.7799735	3.6725249
Number of counts	132.29273	517.29255
Energy (db)	615.14928	290869.4423
Frequency (KHz)	25.098233	19.090999

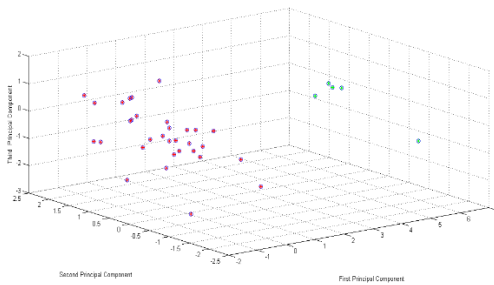
Table 8. Cluster membership

Event Number	Cluster	Distance
1	1	2.263
2	1	1.581
3	1	.838
4	1	1.054
5	1	1.635
6	1	.453
7	1	.886
8	2	.814
9	1	1.404
10	1	1.378
11	1	1.538
12	1	1.956
13	2	.830
14	1	.847
15	1	.559
16	2	1.041
17	1	2.032
18	1	2.805
19	1	1.248
20	1	1.425
21	1	.851
22	1	.910
23	1	1.899
24	1	1.366
25	1	1.281
26	1	.844
27	1	2.657
28	1	2.551

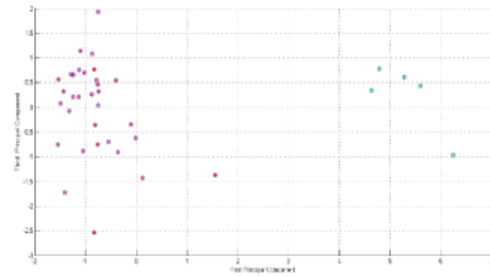
Table 8. Cluster membership (Cont.)

Event Number	Cluster	Distance
29	1	2.024
30	1	3.287
31	2	1.930
32	1	1.015
33	1	.764
34	1	.688
35	2	.783
36	1	.891
37	1	1.139

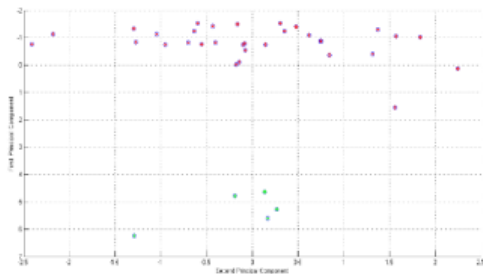
It worth mentioning that the second and the third principal components alone are poorly representing the cluster distribution since they only explain 27.3% of the variance.



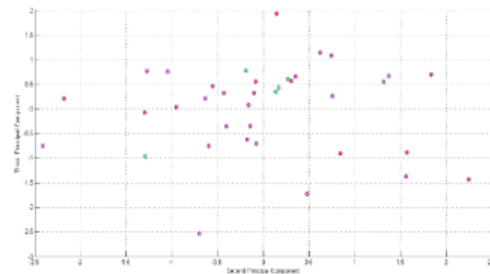
(a) Three principal components contain 97.5 % of variance



(b) First and third principal components contain 81.9 % of variance



(c) First and second principal components contain 85.7 % of variance



(d) Second and third principal components contain 27.3 % of variance

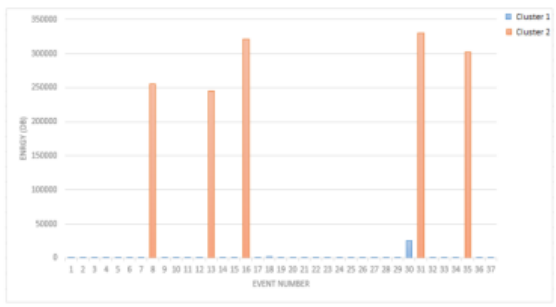
Figure 8 . Principal component projection and clusters distribution for the AE events

Analysis of variance (ANOVA) of the cluster centers (Table 8). As can be seen, most of the means of clustering features differ significantly across the two clusters, because the null hypothesis (means are equal) is rejected in a case at significant level ≤ 0.05 . The frequency is not significant which means it has a little contribution to the cluster solution. The features with large F value provide the greatest separation between clusters. As the F value increases as the importance of feature increases, this was also illustrated in Figure 9.

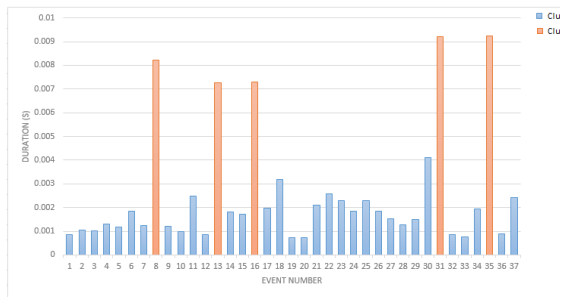
Figure 10 shows waveform samples from cluster one and cluster two. The waveform from cluster one is quite different from the waveform from cluster two, with shorter decay time and less amplitude. The dissimilarities in the events features and waveforms found between the two types of signals lead to the conclusion that the source mechanisms are not the same in both cases.

Table 9. Analysis of variance (ANOVA) of the cluster centers and features importance

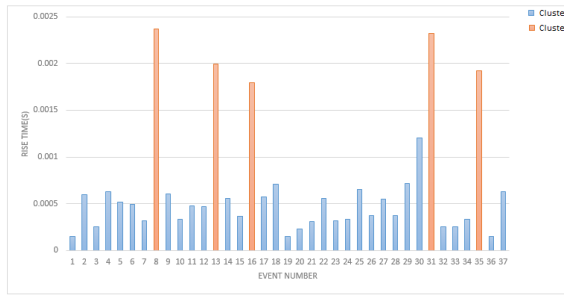
	Cluster		Error		F	Sig.	importance
	Mean Square	df	Mean Square	df			
Rise Time	31.307	1	.134	35	233.503	.000	3
Peak amplitude	25.395	1	.303	35	83.809	.000	5
Duration	32.137	1	.110	35	291.130	.000	2
Kurtosis	7.330	1	.819	35	8.949	.005	6
Number of counts	30.410	1	.160	35	190.403	.000	4
Energy	35.369	1	.018	35	1960.776	.000	1
Frequency	1.481	1	.986	35	1.501	.229	7



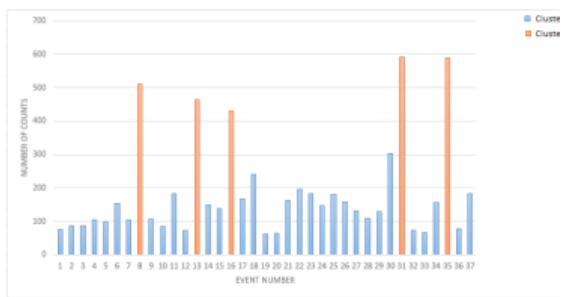
(a) Events in cluster one have less energy



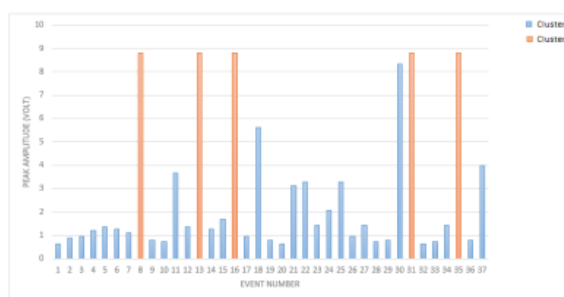
(b) Events in cluster one have shorter duration



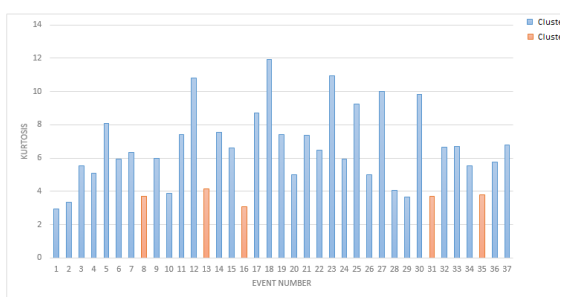
(c) Events in cluster one have faster rise time



(d) Events in cluster one have less number of counts

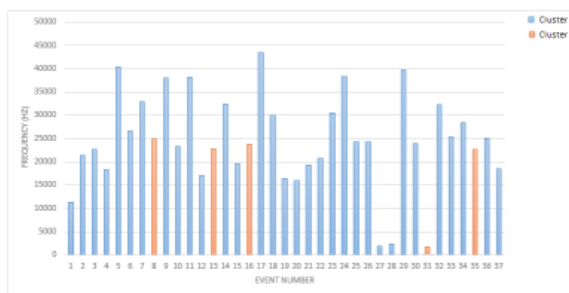


(e) Events in cluster one have smaller amplitude



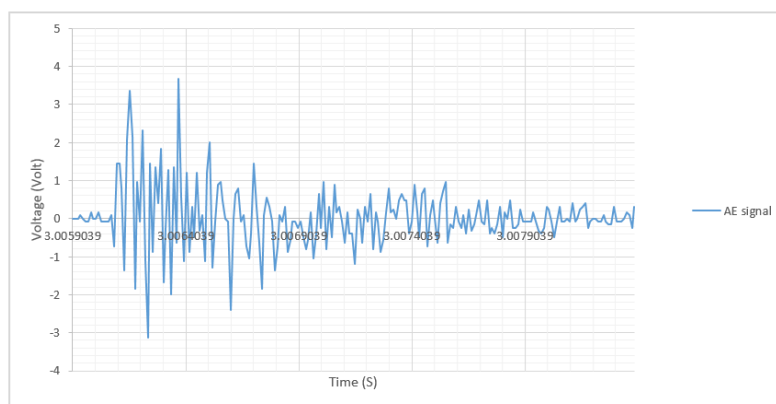
(f) Events in cluster one is peaked distribution

Figure 9 . Comparing the features in clusters one and two the AE events

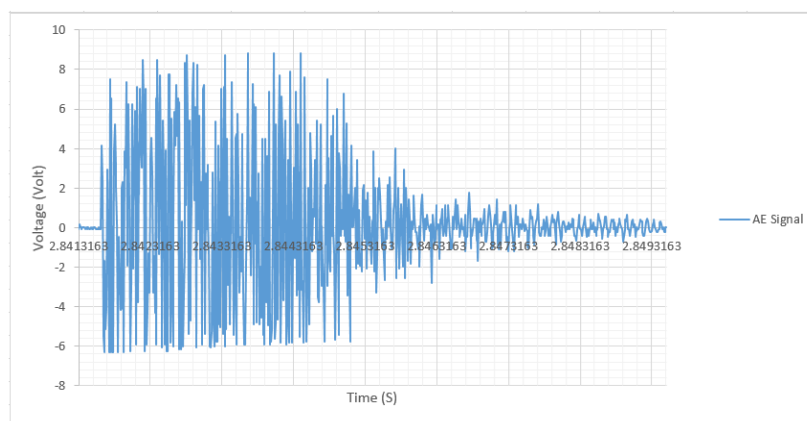


(g) Events in cluster one have larger frequency

Figure 9. Comparing the features in clusters one and two the AE events (Cont.)



(a) Waveform signal sample from cluster one



(b) Waveform signal sample from cluster two

Figure 10 . Comparison between the waveforms from both clusters

3.3. DEFECTS TYPES AND OPTICAL MICROSCOPY STUDY

After preparing the surface of deposited metal, the cracks and pores were observed using an optical microscope, the number of cracks to the number of pores strongly correlated with the number of events in cluster two to the number of events in cluster one. Also, from the literature [10], [23] the waveform and the features of the acoustic emission signal created by cracks is similar to the events in cluster two.

Figure 11 displays cracks caused by thermal stress. The temperature gradient of the deposited layer is large in the direction of thickness during laser deposition process, and the thermal expansion coefficients of the two deposition materials are different, which results in that the thermal stress at the combining surface of deposition, thus the cracks are formed. It also occurs with powder contamination in the powder feeder [21].

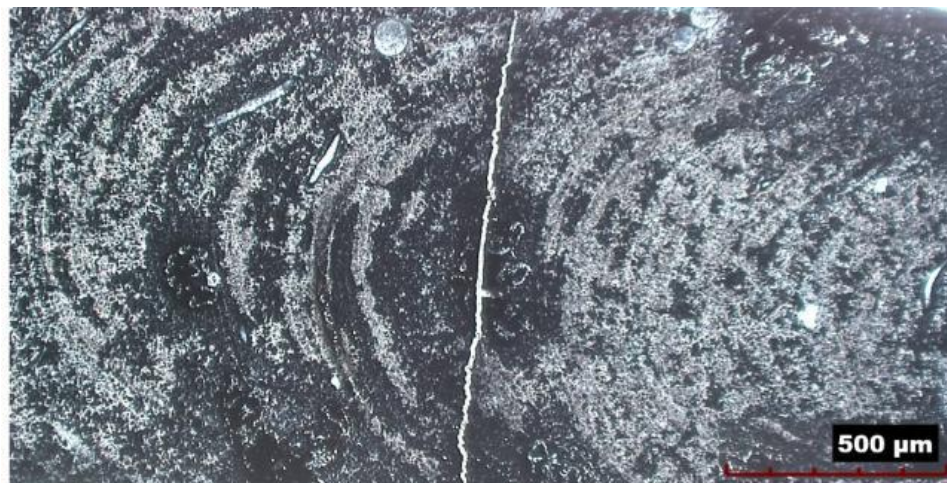


Figure 11. Optical image of a transverse cross-sectioned laser deposit showing a crack and gas porosity

The second type of observed defects is pores which have a spherical form and appear in random locations not associated with the microstructure as shown in Figure 12. The possible sources of these porosities are surface powder contamination [21], gasses trapped within the powder particles due to the difference in the powder sizes, and an oxidation effect since the oxygen level was high due not using the chamber to stimulate defect formation in this research. In fact, surface oxides may most likely remain in the solid state in the melting pool and, as such, upset the wetting mechanisms melted the powder and induces voids.

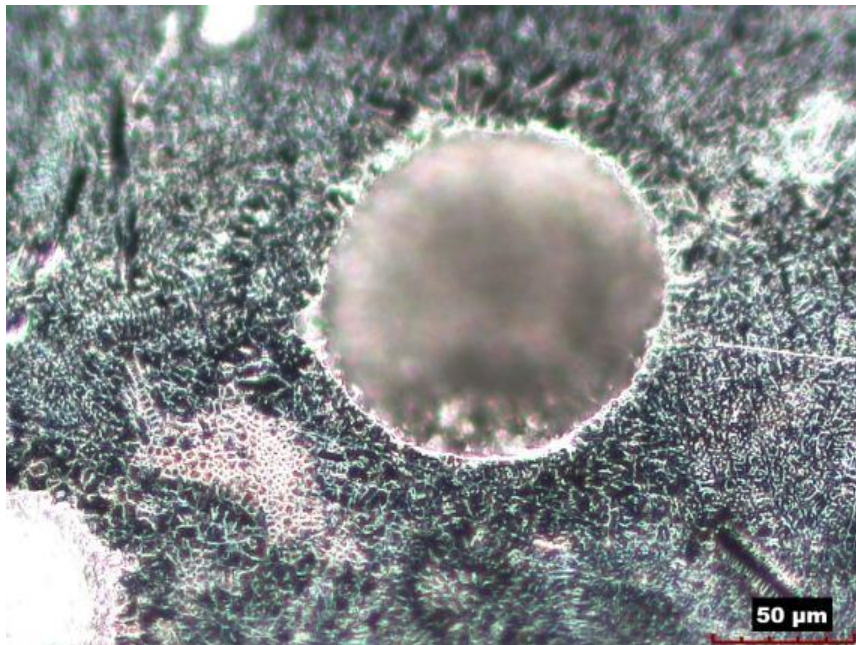


Figure 12. Optical image of a transverse cross-sectioned laser deposit showing a gas porosity

4. CONCLUSIONS

The AE signal was collected during the LMD in an oxidized environment with mixed metal powders to stimulate all possible types of defects. K-Means clustering method was implemented to analyze the AE signals and identify defects source mechanisms. Principal components analysis was used to reduce the dimension of the clustered AE events to facilitate the visualization and representation the clusters in 2D and 3D plots. The results show that there are two clusters associated with distinct defect source mechanisms for the LMD. These clusters can be described by the signal energy, duration, rise time, number of counts, and amplitude, revealing that the signal energy is a crucial feature in identifying the AE defect source mechanisms.

The clustering results successfully distinguish two main defects types and their signal characteristics. Porosities produce the AE signals with shorter decay time and less amplitude. The cracks trigger the AE signals with short durations and high amplitudes. The present study provides a promising method for the discrimination of the defect types in the LMD by using the features content of the AE signals in the time domain.

AE monitoring system has been proposed and proved effective to classify the AE signals with different features associated with various emitting sources. Due to layer-by-layer additive manufacture nature of LMD, the proposed scheme is capable of working in real time. The method is data driven and the number of clusters to be created does not have to be specified in advance, they only depend on the number of defects being created. The validation of the proposed methodology has been carried out using an optical microscope; it showed the correlation between the number of acoustic events and the number of defects determined by post-test optical microscopy. The numbers of signal

events are in each cluster are in agreement with the rough estimations of the associated numbers of defects.

ACKNOWLEDGMENT

This research was supported by the National Science Foundation grants IIP-1345240, CMMI-1301414, and CMMI-1547042. Support from Product Innovation and Engineering, LLC, Missouri S&T Intelligent Systems Center, and the Missouri S&T Manufacturing Engineering Program, is also greatly appreciated.

REFERENCES

- [1] Wang L, Felicelli SD, Craig JE (2009) Experimental and numerical study of the LENS rapid fabrication process. *ASME J Manuf Sci Eng* 131(4):041019–041019-8. doi:[10.1115/1.3173952](https://doi.org/10.1115/1.3173952)
- [2] Weerasinghe V, Steen W (1983) Laser cladding by powder injection. In: *Proc. 1st Int. Conf. Lasers Manuf.*, p 125–132
- [3] Weerasinghe V, Steen W (1987) Laser cladding with blown powder. *Met Constr* 19:581–585
- [4] Sears J (1999) Direct laser powder deposition ‘State of the Art’, No. KAPL-P-000311; K99089, Knolls At. Power Lab., Nis. NY
- [5] McLean M (1997) Laser direct casting high nickel alloy components. *Adv Powder Metall Part Mater* 3:21
- [6] Mazumder J, Choi J, Nagarathnam J, Koch K, Hetzner D (1997) The direct metal deposition of H13 tool steel for 3D components. *JOM* 49:55–60
- [7] Lewis G, Nemec R, Milewski J, Thoma D (1994) Directed light fabrication, No. LAUR-94-2845; CONF-9410189-2, Los Alamos Natl. Lab., NM, US
- [8] Milewski J, Lewis G, Thoma D (1998) Directed light fabrication of a solid metal hemisphere using 5-axis powder deposition. *J Mater Process Technol* 75:165–172

- [9] Wu X, Liang J, Mei J, Mitchell C, Goodwin PS, Voice W (2004) Microstructures of laser-deposited Ti-6Al-4V. *Mater Des* 25:137–144
- [10] Arcella F, Froes F (2000) Producing titanium aerospace components from powder using laser forming. *JOM* 52:28–30
- [11] Fessler J, Merz R (1996) Laser deposition of metals for shape deposition manufacturing, In: *Proc Solid Free Fabr Symp, Univ Texas, Austin, 1996*, pp. 117–124
- [12] Keicher DM, Miller WD (1998) LENS moves beyond RP to direct fabrication. *Met Powder Rep* 53:26–28
- [13] Griffith M, Schlienger M, Harwell L (1998) Thermal behavior in the LENS process, No. SAND-98-1850C; CONF-980826-, Sandia Natl. Labs, Albuquerque, NM, USA
- [14] Xue L, Islam M (1998) Free-form laser consolidation for producing functional metallic components. *Laser Inst. Am. Laser Mater Process* 84
- [15] Xue L, Islam M (2000) Free-form laser consolidation for producing metallurgically sound and functional components. *J Laser Appl* 12: 160–165
- [16] Ma Z, Sun G, Liu D, Xing X (2016) Dissipativity analysis for discrete-time fuzzy neural networks with leakage and timevarying delays. *Neurocomputing* 175 :579–584 Part A
- [17] Liao Z, Axinte DA (2016) On monitoring chip formation, penetration depth and cutting malfunctions in bone micro-drilling via acoustic emission. *J Mater Process Technol* 229:82–93
- [18] Gaja H, Liou F (2016) Automatic detection of depth of cut during end milling operation using acoustic emission sensor. *Int J Adv Manuf Technol*
- [19] Gutkin R, Green CJ, Vangrattanachai S, Pinho ST, Robinson P, Curtis PT (2011) On acoustic emission for failure investigation in CFRP: pattern recognition and peak frequency analyses. *Mech Syst Signal Process* 25(4):1393–1407
- [20] Rousseeuw PJ (1987) Silhouettes A: a graphical aid to the interpretation and validation of cluster analysis. *J Comput Appl Math* 20:53–65
- [21] Barua S ((2014)) Vision-based defect detection in laser metal deposition process. *Rapid Prototyp J* 20(1):77–85

III. DEFECTS CLASSIFICATION OF LASER METAL DEPOSITION USING LOGISTIC REGRESSION AND ARTIFICIAL NEURAL NETWORKS FOR PATTERN RECOGNITION

Haythem Gaja ^{*a}, Frank Liou ^a

^aMissouri University of Science and Technology, Mechanical & Aerospace Engineering,
400 W 13th Street, Rolla, MO 65409-0050, USA

ABSTRACT

Detecting laser metal deposition (LMD) defects is a key element of evaluating the probability of failure of the produced part. Acoustic emission (AE) is an effective technique in LMD defect detection. This work presents a systematic experimental investigation of using AE technique for detecting and classifying different defects in LMD. The defects generated during LMD simulate AE sources on deposited material while the AE sensor was mounted on the substrate to capture AE signals. An experiment was conducted to investigate the ability of AE to detect and identify defects generated during LMD using a logistic regression (LM) model and an artificial neural network (ANN). AE features, such as peak amplitude, rise time, duration, energy, and number of counts along with statistical features were extracted and analyzed. Additionally, frequency analysis using fast Fourier transformation was conducted on the AE signal. The results show that AE has considerable potential in LMD monitoring for assessing the overall deposition quality and identifying defects that can significantly reduce the strength and reliability of deposited material, and consequently, increase the risk of a component's failure.

Keywords: Laser metal deposition - Deposition defects- Acoustic emission- Artificial neural network - Logistic regression - Machine learning

1. INTRODUCTION

Laser metal deposition (LMD) is an advanced additive manufacturing (AM) process used to build or repair metal parts layer-by-layer for a range of different applications. Any presence of deposition defects in the part produced causes change in the mechanical properties that might cause failure to the part. Using remedies to fix these defects will increase the machining time and costs. Monitoring the LMD process is crucial for detecting any undesired defects in the produced part and for avoiding corrective actions. Therefore, early detection is critical. Because different defect mechanisms can produce similar waveforms, the analysis and the modeling of the acoustic emission signals during the deposition process are essential, and an online detection system of any significant changes in those signals is required to detect these changes.

LMD is one type of powder-based laser deposition additive manufacturing techniques such as laser cladding [2, 3], laser direct casting [4, 5], direct metal deposition [6], directed light fabrication [7, 8, 9], laser forming [10], shape deposition manufacturing [11], laser engineered net shaping [12,13], free-form laser consolidation [14,15], and many others. The main process parameters of LMD are laser power, travel velocity, and powder flow rate. These parameters control the geometry accuracy and the mechanical properties of the finished part by determining the size of the molten pool, the part deformation, and the microstructure of the deposited layers. Additionally, they affect

the temperature profile and cooling rate in the molten pool, as well as the thermal cycles at each location of the fabricated part [1].

The acoustic emission sensor is a piezoelectric transducer that generates an electrical charge in response to the elastic waves emitted from sources inside of a material as a result of a sudden release of energy. The AE technique is one of most powerful monitoring technologies available ; it has been used for monitoring in many manufacturing processes such as the cutting operations [16,17,18] and the welding process. Jolly [19] monitored the crack growth in stainless steel welds, and it was found that a maximum AE rate is directly related to the number of cracks in the weld defect zone. This work is considered to be the first significant milestone in the application of the AE technique for monitoring the welding process. A.S.Sun. Rostek [20] in 1990 used computer-aided acoustic pattern recognition to demonstrate the monitoring capabilities of acoustic signals. Duley and Mao [21] studied the laser welding process of aluminum 1100 using acoustic emission. They found that a keyhole could be identified by a specific AE frequency component, and they could then correlate the AE with laser penetration and surface condition. Grad et al. [22] in 1996 developed a monitoring method that uses different statistical parameters to assess process stability.

Bohemen [23] demonstrated that martensite formation during gas tungsten arc (GTA) welding of steel 42CrMo4 can be monitored by means of AE. It was shown that a particular relation exists between the root mean square (RMS) value of the measured AE and the volume rate of the martensite formation during GTA welding. Grad et al. [24] examined the acoustic waves generated during the short circuit gas metal arc welding

process. It was found that the acoustic method could be used to assess welding process stability and to detect the severe discrepancies in arc behavior.

Yang [25] used an acoustic emission (AE) sensor to identify damage in metallic materials. Results suggested a strong correlation between AE features (i.e., RMS value of the reconstructed acoustic emission signal), surface burn, residual stress value, and hardness of steels. Diego-Vallejo [26] found that the focus position, as an important parameter in the laser material interactions, changes the dynamics and geometric profile of the machined surface as well as the statistical properties of the measured AE signal.

Wang [27] utilized acoustic emission testing to identify crack location using two acoustic emission sensors during laser cladding process. The temperature ranges of crack generation and expansion were studied using finite element analysis (FEA). The forms and extended forms of the cracks were investigated by using an optical microscope and scanning electron microscope (SEM). However, the characteristic of the acoustic emission and the features of the signal were not studied, and the microscopy investigation of cracks was not linked to the location of the cracks results. The experiment and analysis results show that the amount of cracks increases with the area and thickness of the coating and the cooling rate increasing.

Recently, Siracusano [28] proposed a framework for the evaluation of material damages based on the Hilbert–Huang Transform, and this framework facilitates the systematic employment of both established and promising analysis criteria. The framework also provides unsupervised tools to achieve an accurate classification of the fracture type. Bianchi [29] suggested a wavelet packet decomposition within the framework of multiresolution analysis theory should be considered for analyzing acoustic

emission signals when investigating the failure of rail-wheel contact within a fatigue and wear study. The application was shown to be adequate for analyzing such signals and filtering out their noise during real-time monitoring.

However, more research is needed to develop a technique that uses AE as a reliable measure for LMD defect detection and integrity assessment. In this paper, the defect type distinguishing of LMD is investigated by modeling the AE signals. The AE technique is suitable for examining the defect sources during LMD; it contains rich defect-related information such as crack and pore formation, nucleation, and propagation. Information on defect development is difficult to obtain by only using the AE waveform in a time domain. Thus, other features such as amplitude, energy, rise time, count and frequency, are extracted to analyze qualitative defect mechanisms. The purpose of the present work is to develop reliable prediction models of defect classification that are based on AE data acquired during LMD.

This work used logistic regression and an artificial neural network to represent the relationship between the AE signal and the defect types in LMD processes, and then the results of the two models were compared with the results of clustering analysis. The AE event features were fed into the two models to measure operation quality during LMD. After the models had been trained, the inference system classified the AE events in real time from the experimental sensor signal. The results of the monitoring algorithm can warn the operator to take corrective actions in order to reach the optimum quality of the produced part.

2. EXPERIMENTS AND DATA COLLECTION

Figure 1 shows a schematic diagram of the experimental set-up. The YAG laser was attached to a 5-Axis vertical computer numerical control machine that is used for post-process machining after LMD. The data acquisition system consists of acoustic emission sensor, coupler, and data acquisition oscilloscope. The used AE system (Kistler 8152B111) has a relatively superior signal-to-noise ratio and sensitivity at the ultra-precision scale. The noise level is much smaller than the signals of interest, also a frequency filtering was used which allowing of passing only those signals falling within a selected bandwidth.

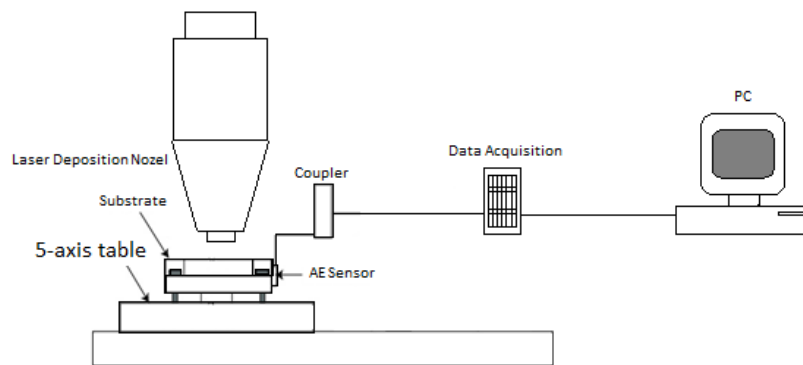


Figure 1. Experimental setup shown the LMD system and ae data acquisition system

The acoustic emission sensor is made up of the sensor housing, a piezoelectric sensing element, and a built-in impedance converter. The sensing element, made of piezoelectric ceramic, is mounted on a thin steel diaphragm. Its construction determines the sensitivity and frequency response of the sensor. It is acoustically isolated from the housing by design and therefore well protected against external noise. The acoustic

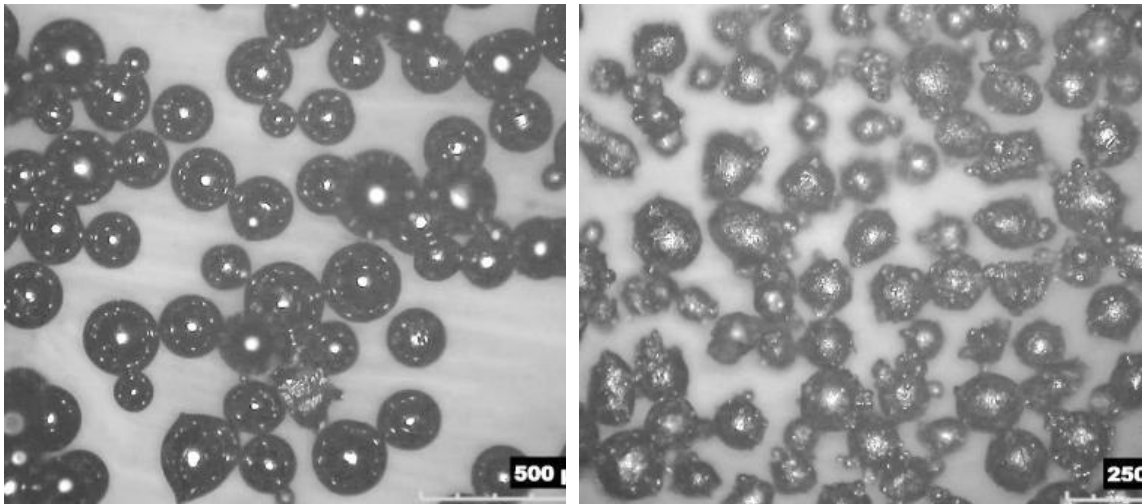
emission sensor is highly sensitive to surface and longitudinal waves over a broad frequency range.

The AE-Piezotron coupler comprises plug-in modules that amplify and filter the raw signal. The main function of the coupler is to supply power to the sensor and process the emission signal. The gain factor, low and high pass filters, and integration time constant are included in one electronic board, allowing the best possible adaptation to a specific monitoring function. The coupler provided 0–5 V voltage signals proportional to the detected defect and eliminated any need for further signal processing. Figure 3.3 shows the coupler assembly diagram.

Picoscope 2205A works as a dual-channel oscilloscope to capture the AE signal and stream it to a computer for further analysis. The oscilloscope measures the change in the acoustic emission signal over time, and helps in displaying the signal as a waveform in a graph. The raw signals were first fed through the data acquisition system and then processed and recorded using the Matlab software.

A powder feeder system was used to deliver the atomized powder to the melt pool using argon gas (which is also used as a shielding gas), and it flowed through channels in the nozzle of laser deposition head to reduce the oxidation of the deposit. During the laser metal deposition process, porosities and cracks can be formed as the result of a lack of fusion, shield gas trapping, and the difference in thermal coefficients of the deposited material and the substrate. The AE signal was recorded during a laser deposition process in an oxidized environment and with contaminated powder in order to induce pores and cracks as a result of thermal coefficient difference. The material of the substrate was tool steel. Cracks and porosities were simulated primarily by mixing the Ti-6Al-4V powder

with H13 tool steel powder. The two powders particles as illustrated in Figure 2 are non-uniform in shape and size and may contain internal voids that can cause deposition defects when mixed. Table 1 displays the chemical composition and the thermal properties of both powders.



(a) Ti-6Al-4V metal powder

(b) H13 metal powder

Figure 2. Optical image of the metal powders used in deposition process

Table 1. The composition and thermal properties of titanium and tool steel metallic powders (mass %)

	Ti-6Al-4V	H13
Iron, Fe	< 0.25	Balance
Chromium, Cr	-	4.75 – 5.5
Molybdenum, Mo	-	1.1 – 1.75
Silicon, Si	-	0.80-1.20
Vanadium, V	3.50 to 4.50	0.80-1.20
Carbon, C	< 0.08	0.32-0.45
Nickel, Ni	-	0.3
Manganese, Mn	-	0.20-0.50
Titanium, Ti	Balance	-
Aluminum, Al	5.50 to 6.50	-
Thermal expansion ($^{\circ}\text{K}^{-1}$)	11×10^{-6} - 15×10^{-6}	13×10^{-6} - 16×10^{-6}
Thermal conductivity (W/mK)	8	28.6

AE signal with enough features is critical in order to collect as much information as possible about the emitting source, especially when there is little literature regarding the use of AE techniques for monitoring LMD process that can be utilized as a reference during AE feature selection. The AE signal can be represented in the frequency domain by using fast Fourier transform (FFT) or in the time domain by using peak amplitude, kurtosis, energy, number of counts, duration, and rise time. Figure 3 shows some of the time-dependent features (Table 2).

Table 2. Time domain and frequency domain AE signal features

Feature	Definition
Peak Amplitude	It is the greatest measured voltage in an AE event
kurtosis	It is a measure of whether the data of an AE event are peaked or flat compared to a normal distribution. $\text{Kurtosis} = \frac{\sum_{i=1}^N (x_i - \bar{x})^2 / N}{\sigma^4} - 3 \quad (1)$ Where N is the number of samples (x_i) in an AE signal, σ is the standard deviation, and \bar{x} is the mean.
Energy	Since the domain of the AE event signal is discrete, the energy of the signal is given by $\text{Energy} = \sum_{i=1}^N (x_i)^2 \quad (2)$
Number of Counts	It is the number of pulses emitted by the AE event.
Duration	It is the time difference between the first and last threshold crossings.
Rise Time	It is the time interval between the first threshold crossing and the AE event peak.
Peak Amplitude Frequency	It is a characterization of the magnitude and frequency of an AE event using Fast Fourier transform

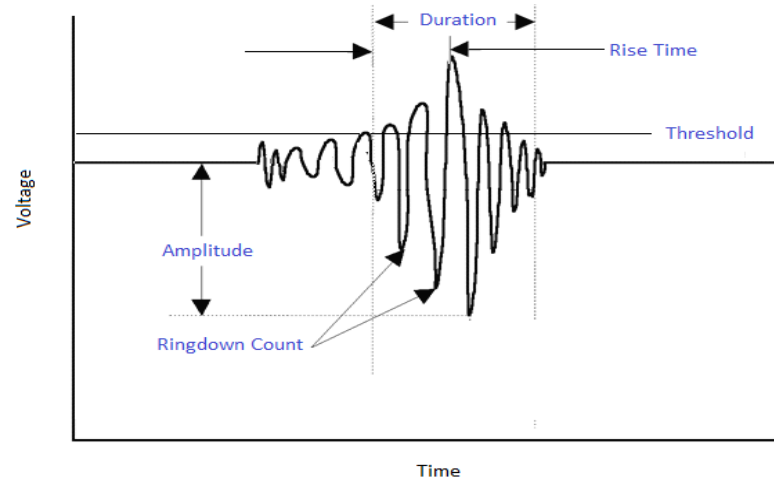


Figure 3. Time dependent AE event features

Among all of the features, the signal amplitude alone was measured in real time by the data acquisition system. Once the AE signal is recorded, the other features were calculated from the waveforms at the end of the deposited layer because they are particularly dependent on the amplitude and threshold. In this work, all of these features were used in a multi-logistic regression statistical analysis and ANN analysis. No AE noise associated with the operation of the laser system or the CNC system was observed. Also, it was found in this study that the noise level is much smaller than the signals of interest. Additionally, a frequency filtering was used, which allowed only those signals falling within a selected bandwidth (100 kHz to 900 kHz) to pass through the filter.

Two depositions were performed with standard parameters for depositing titanium powder, as shown in Table 3. The first deposit was 15 mm in length and the second deposit was 5 mm in length. The first AE signal was used to group the AE events into homogeneous subgroups (clusters), and the experiment conditions, data collection, and

results were discussed in detail in a previous study by the authors [30]. In this previous study, the results were used to construct the LR and the ANN models.

Table 4 shows the AE event features and results of the signal analysis. The number of pores in the first signal was 32, while the number of cracks was found to be only 5. This data was used to create LR and ANN models. To validate how well the two models fit the data, a second AE signal was acquired under the same experimental conditions. The second set of the AE signal was used in this study to estimate the probability of a binary response crack or pore (0 or 1) based on the features of the AE events. The outcomes of the two models were compared and verified with the second AE signal.

Figure 4 illustrates the main steps in the developed procedure that was used to analyze the AE data. The AE sensor was attached to a substrate to transform the energy released by the laser deposition into an acoustic emission signal. The formation of porosities and cracks generates an acoustic emission signal, which is an elastic wave that travels from the source toward a sensor, moving through the substrate until it arrives at

Table 3. Laser metal deposition process parameters

Parameter	Value
Laser power	1,000 Watt
Powder feed rate	10 g/min
Table velocity	300 mm/min
Layer thickness	About 0.5 mm
Layer width	About 2.5 mm

Table 4. Standardized AE signal features and the clustering results

Event Number	Rise Time	Peak amplitude	Duration	Kurtosis
1	-0.8632828	-0.7341107	-0.68626	-1.44472
2	-0.1261721	-0.6508765	-0.60598	-1.25783
3	-0.6931803	-0.6231318	-0.62959	-0.34811
4	-0.0694712	-0.5398975	-0.51153	-0.52405
5	-0.2584740	-0.4844081	-0.55876	0.728254
6	-0.2962745	-0.5121528	-0.28959	-0.16773
7	-0.5797787	-0.5676423	-0.53514	0.00428
8	2.803370	2.0958524	2.3407	-1.1222
9	-0.1072718	-0.6786212	-0.53987	-0.14773
10	-0.5608784	-0.7063660	-0.64376	-1.04886
11	-0.3151748	0.3201892	-0.02042	0.449555
12	-0.3340751	-0.4844081	-0.68626	1.881232
13	2.1796615	2.0958524	1.953476	-0.93525
14	-0.1828729	-0.5121528	-0.29903	0.510621
15	-0.5041776	-0.3734291	-0.33681	0.103122
16	1.8583568	2.0958524	1.967643	-1.38266
17	-0.1639726	-0.6231318	-0.23292	0.998504
18	0.0628306	0.9860629	0.267636	2.358211
19	-0.8632828	-0.6786212	-0.74765	0.445735
20	-0.7309809	-0.734110	-0.7382	-0.56879
21	-0.5986790	0.1259761	-0.17625	0.437646
22	-0.1828729	0.1814655	0.02208	0.054488
23	-0.5797787	-0.4566633	-0.1007	1.929897
24	-0.5608784	-0.234705	-0.28487	-0.16722
25	-0.0316707	0.1814655	-0.09598	1.216332
26	-0.4852773	-0.6231318	-0.28487	-0.57514
27	-0.2017732	-0.4566633	-0.41237	1.534873
28	-0.4852773	-0.7063660	-0.51626	-0.96409
29	0.0817309	-0.6786212	-0.42653	-1.13012
30	0.8755425	1.9293840	0.65486	1.466014
31	2.7277695	2.0958524	2.760979	-1.11484
32	-0.6931803	-0.734110	-0.69098	0.127625
33	-0.6931803	-0.7063660	-0.72403	0.144849
34	-0.5608784	-0.4566633	-0.23764	-0.33667
35	2.066259	2.0958524	2.765701	-1.07521
36	-0.8632828	-0.6786212	-0.67209	-0.25692
37	-0.0694712	0.4311682	-0.04875	0.176898

Table 4. Standardized AE signal features and the clustering results (Cont.)

Event Number	Number of counts	Energy	Frequency	Defect
1	-0.75435274	-0.42589	-1.27045	Pore
2	-0.6648721	-0.42121	-0.28512	Pore
3	-0.6786384	-0.42337	-0.16714	Pore
4	-0.5478591	-0.41726	-0.57824	Pore
5	-0.5960409	-0.4176	1.576003	Pore
6	-0.2174693	-0.41689	0.226959	Pore
7	-0.5547422	-0.42265	0.843153	Pore
8	2.2535706	2.41352	0.053381	Crack
9	-0.5409760	-0.42517	1.349834	Pore
10	-0.6924046	-0.42553	-0.08978	Pore
11	-0.0109757	-0.31195	1.354937	Pore
12	-0.7612358	-0.42228	-0.71316	Pore
13	1.9231809	1.795566	-0.14501	Crack
14	-0.2381187	-0.41256	0.799576	Pore
15	-0.3138330	-0.40788	-0.4526	Pore
16	1.7029210	2.668412	-0.04808	Crack
17	-0.1142225	-0.42121	1.881284	Pore
18	0.3882451	-0.26322	0.568001	Pore
19	-0.8438333	-0.42517	-0.77585	Pore
20	-0.8300670	-0.42589	-0.82462	Pore
21	-0.1555213	-0.35378	-0.48302	Pore
22	0.0785047	-0.33756	-0.34344	Pore
23	-0.0109757	-0.38877	0.603812	Pore
24	-0.2587681	-0.39165	1.376322	Pore
25	-0.0316251	-0.36316	-0.00579	Pore
26	-0.1761706	-0.42337	-0.00107	Pore
27	-0.3620149	-0.4212	-2.1943	Pore
28	-0.5203266	-0.42445	-2.15717	Pore
29	-0.3757811	-0.42517	1.515988	Pore
30	0.8218817	0.066326	-0.03145	Pore
31	2.8042202	2.811349	-2.23613	Crack
32	-0.7612358	-0.42589	0.776849	Pore
33	-0.8094177	-0.42553	0.102579	Pore
34	-0.1899369	-0.40212	0.40919	Pore
35	2.7835709	2.630087	-0.15449	Crack
36	-0.7337033	-0.42517	0.082367	Pore
37	-0.0109757	-0.2917	-0.56332	Pore

the acoustic emission sensor. In response, the sensor produces an electrical signal, which is passed to electronic equipment for further processing and defect detection. Since the LMD is an additive process and it deposits metals layer by layer, the AE signal was recorded for each layer and analyzed in order to extract any useful information from the AE events.

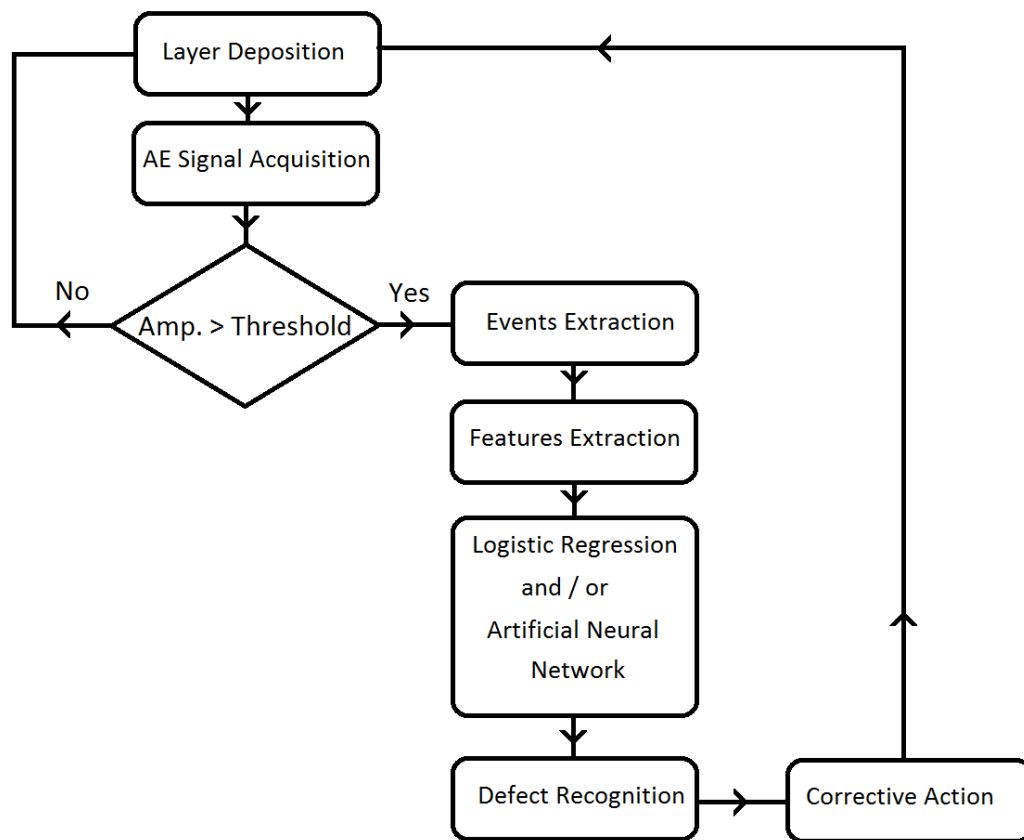


Figure 4. Step-by-step operations used to perform the acoustic emission analyses

3. RESULTS AND DISCUSSION

3.1. LOGISTIC REGRESSION-BASED MODELING

In logistic regression, the dependent variable is binary, meaning that it can take only two values of "0" and "1", where 0 represents defect type I and 01 represents defect type II. Each of these results represents the outcomes of crack or pore, respectively. Cox [31] developed the logistic regression in 1958. The LR model is used to estimate the probability of a binary response (defect type) based on seven variables (AE event features).

Logistic regression is used to model the probability of defect classification into a type I or type II defect. Let y^* indicate the classification of the i^{th} AE event such that $Y_i^* = 1$ if the AE event is classified as pore and $Y_i^* = 0$ if the AE event is classified as crack:

$$y^* = \ln\left(\frac{p}{1-p}\right) = \beta_0 + \sum_{i=1}^n \beta_i x_i \quad (1)$$

Table 5. Results of the regression analysis

Term	Coefficients	Standard Error	P-value
Intercept	-12.2018419	0.0805	<0.001
x ₁	2.37719998	0.2926	<0.001
x ₂	-4.78228419	0.2341	<0.001
x ₃	46.23988958	3.112	<0.001
x ₄	0.116482205	0.09162	0.06
x ₅	-34.48089538	2.429	<0.001
x ₆	4.919644537	0.8852	<0.001
x ₇	-0.06002589	0.07432	0.217

Therefore, the probability (p) of the porosity defect being formed is

$$p = \left(\frac{e^{y^*}}{1+e^{y^*}} \right) \quad (2)$$

In Table 5, x_1 , x_2 , x_3 , x_4 , x_5 , x_6 , and x_7 represent rise time, peak amplitude, duration, kurtosis, number of counts, energy, and frequency, respectively. By considering all terms, the LR model for defect formation is

$$y^* = \ln \left(\frac{p}{1-p} \right) = -12.2 + 2.37 x_1 - 4.78x_2 + 46.23 x_3 + 0.11 x_4 - 34.48 x_5 + 4.91x_6 - 0.06 x_7 \quad (3)$$

3.2. ARTIFICIAL NEURAL NETWORK BASED MODELING

An ANN is a statistical machine-learning tool established on the idea of how neurons in a human brain work. The neural network consists of layers and nodes, called neurons, and the number of layers and neurons depends on the difficulty of the problem being modeled. The input and output layers have neurons equal to the number of the inputs and the outputs, respectively. The neurons are connected by synapses, which take a value from an input neuron, multiply it by a specific weight, and output the results. The neurons have a more complicated purpose: they add together all outputs from all synapses and apply an activation function.

A sigmoid function was used for activation. This kind of function was selected because it is one of the common types of transformation functions and because it

provides a method of establishing complex, nonlinear relationships between the input and output data sets, as shown in Figure 5. A sigmoid function was used to map the output of the hidden layer to the range of values of (0, 1).

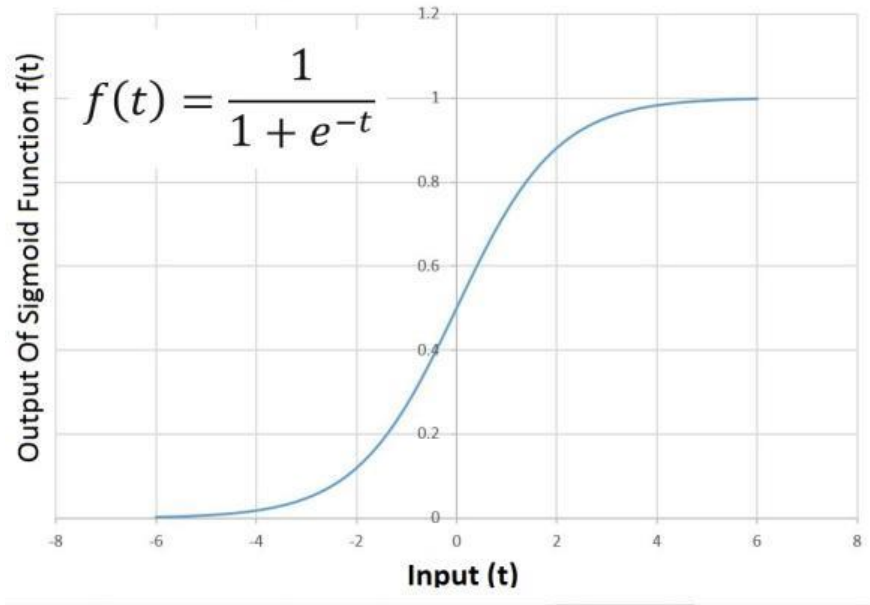


Figure 5. Sigmoid activation function

Any ANN has at least three layers: an input layer, a hidden layer, and an output layer. If X is the input data vector (which in this work is a one by seven vectors as shown in Figure 6), $W(1)$ is the weight matrix (which is a seven by N matrix, where N is the number of neurons in the hidden layer), and $Z(2)$ is the transfer function of the second layer:

$$Z^{(2)} = X \times W^{(1)} \quad (4)$$

By applying transfer function to each element in $Z^{(2)}$, $a^{(2)}$ activation function of the second layer can be obtained by

$$a^{(2)} = f(Z^{(2)}) \quad (5)$$

where $a^{(2)}$ has the same size as $Z^{(2)}$. By multiplying weight matrix of the second layer $W^{(2)}$ (which is an N by one matrix), there is only one output in our ANN which is defect type

$$Z^{(3)} = a^{(2)} \times W^{(2)} \quad (6)$$

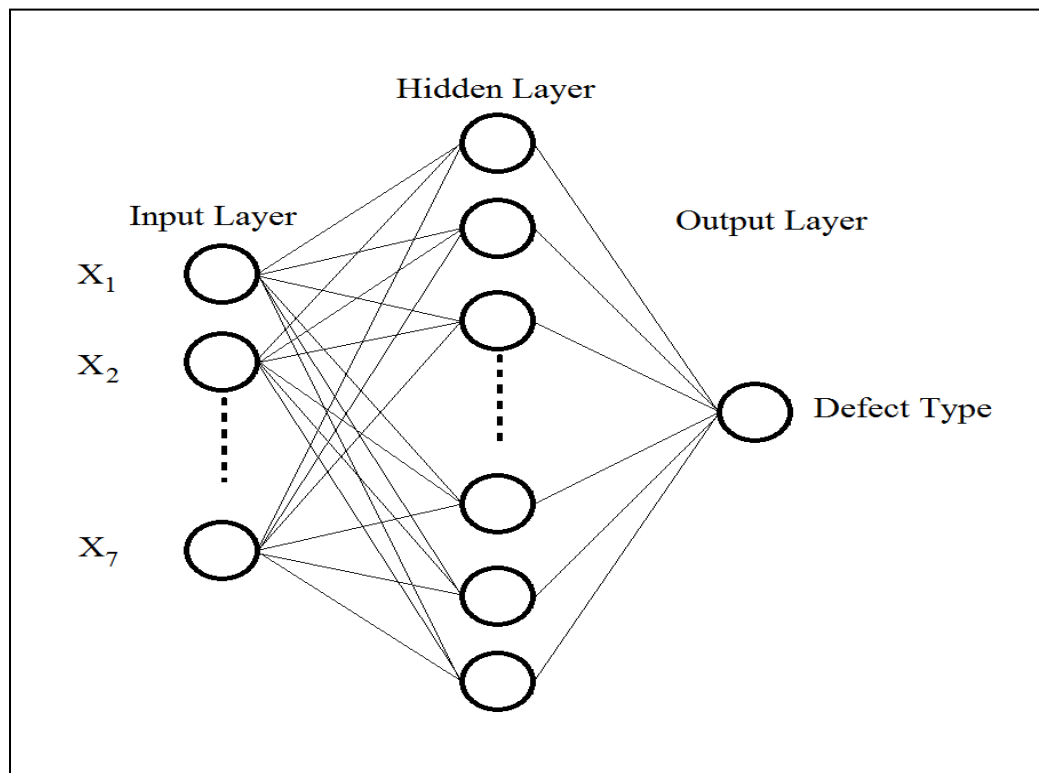


Figure 6. Neural network architecture

where $Z^{(3)}$ is the transfer function of the third layer. Finally, the activation function is applied to $Z^{(3)}$ to obtain the estimate for defect type y' :

$$y' = f(Z^{(3)}) \quad (7)$$

Without training, the network's estimation error will be very large, as training is the process of updating the weight matrix in order to minimize the cost function J

$$J = \sum \frac{1}{2} (y - y')^2 \quad (8)$$

One of the training algorithms that can be used to train the ANN is a supervised learning algorithm called a backpropagation algorithm. This algorithm adjusts the learning rate and momentum coefficient and keeps them between 0 and 1. Equation 8 can be written as

$$J = \sum \frac{1}{2} (y - f(f(XW^{(1)})W^{(2)}))^2 \quad (9)$$

In order to save time and reduce calculations, the gradient descent method is used to guarantee that the search for J is in the correct direction and stop the search when the smallest J is reached (i.e., when the cost function stops decreasing). These tasks are accomplished by taking the partial derivative of J with respect to W ($\frac{\partial J}{\partial W}$) so that $\frac{\partial J}{\partial W}$ is positive (the cost function is increasing) and vice versa. This method is useful, especially for multidimensional problems. Gradient descent can be performed either after using all

training data (batch gradient descent) or after each input–output pair is identified (sequential gradient descent).

The neural network was trained with 25 data points (AE signal features) to estimate the weights (included biases) of candidate designs, and six data points were used to both estimate the non-training performance error of candidate designs and stop the training once the non-training validation error estimate stopped decreasing. Also, six data points were used as testing data to obtain an unbiased estimate of the predicted error of unseen non-training data. Training, validation and testing data were randomly chosen from different cutting conditions from the data set that consisted of 37 data points (AE signal features).

Figure 7 illustrates the mean square error versus iteration (Epochs) number while using the Bayesian regularization-training algorithm. 25 neurons were used within the hidden layer in this work. The network was trained for 30 iterations, at which time the performance was changed dramatically, and the best performance was 0.000661 at epoch 18.

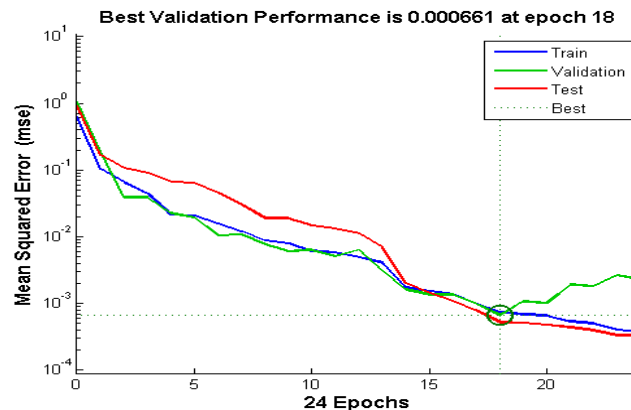


Figure 7. Neural network performance

Table 6. Results of the logistic regression and neural network analysis

Event Number	y^*	LR probability	ANN	Defect
1	2.18E+01	1	1	1
2	2.23E+01	1	1	1
3	2.25E+01	1	1	1
4	2.25E+01	1	1	1
5	2.33E+01	1	1	1
6	2.38E+01	1	1	1
7	2.29E+01	1	1	1
8	-3.40E+01	1.66E-15	3.42E-07	0
9	2.36E+01	1	1	1
10	2.25E+01	1	1	1
11	2.16E+01	1	1	1
12	2.32E+01	1	1	1
13	-1.92E+01	4.44E-09	2.16E-06	0
14	2.34E+01	1	1	1
15	2.29E+01	1	1	1
16	-4.00E+01	4.18E-18	1.17E-06	0
17	2.42E+01	1	1	1
18	2.61E+01	1	1	1
19	2.16E+01	1	1	1
20	2.15E+01	1	1	1
21	2.31E+01	1	1	1
22	2.24E+01	1	1	1
23	2.12E+01	1	1	1
24	2.32E+01	1	1	1
25	2.48E+01	1	1	1
26	2.44E+01	1	1	1
27	2.47E+01	1	1	1
29	2.45E+01	1	1	1
30	2.60E+01	1	0.999998	1
31	-3.97E+01	6E-18	1.96E-07	0
34	2.20E+01	1	1	1
35	-3.92E+01	9.74E-18	3.90E-07	0
36	2.21E+01	1	1	1
37	2.39E+01	1	1	1

The defects are denoted in Table 6 as a binary variable (0 or 1), where 1 represents pores, and 0 represents cracks. The mean squared error (MSE) for the LR model was 1.72973, and the error for the ANN model was 1.702703, where the ideal value of MSE is zero. The MSE defines the average of the squares of residuals, which are found when the values predicted by LR and ANN deviate from the actual values of data. In this study, the performance of the ANN model was slightly better than the LR model. Because there is an insignificant difference in the performance of the two models, they will both be used to estimate the type of defect.

3.3. MODELS VERIFICATION (DEFECTS CLASSIFICATION)

Figure 8 shows an AE signal acquired during the LMD process in the presence of defects. The spikes in the signal are called events, and these have features that are different from the rest of the AE signal. The AE event is counted when the amplitude of the signal is higher than a preset threshold and is preceded and followed by a signal with amplitude lower than the threshold for a specified period.

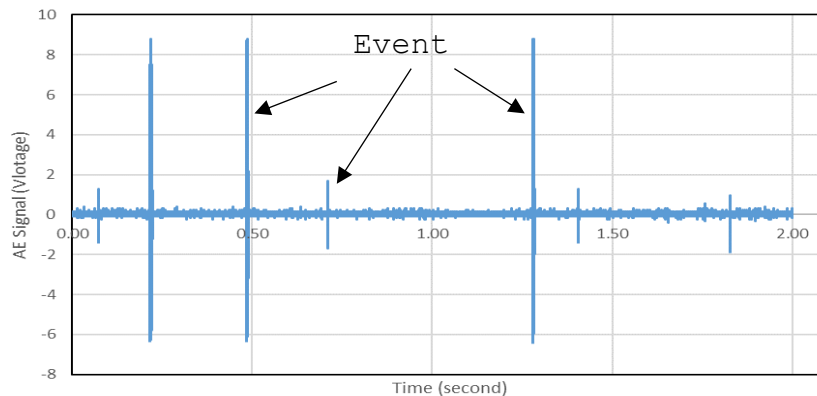


Figure 8. AE raw signal acquired during LMD process

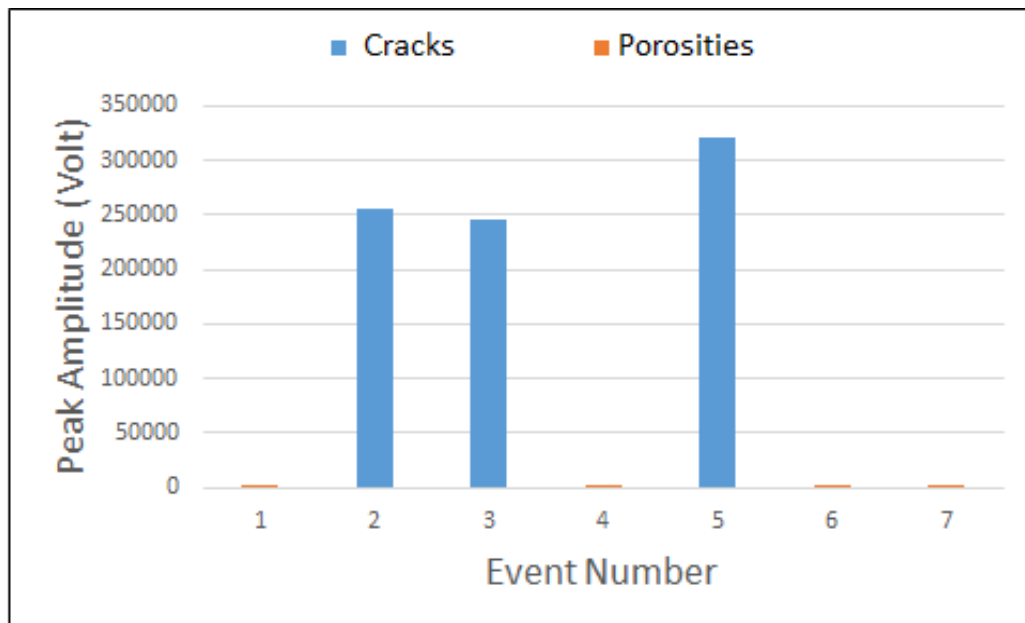
Table 7 shows the outcomes of logistic regression and neural network analysis compared to clustering analysis. Both models succeed at predicting the type of defect, and the AE signal contained three cracks and four pores.

As seen in Figure 9, most of the features of AE events differ significantly between the two types of defects. The signal energy is the most significant feature, which means it has the most contribution to the defect classification (Figure 9.a). The features in the figure provide the greatest separation between the two defects.

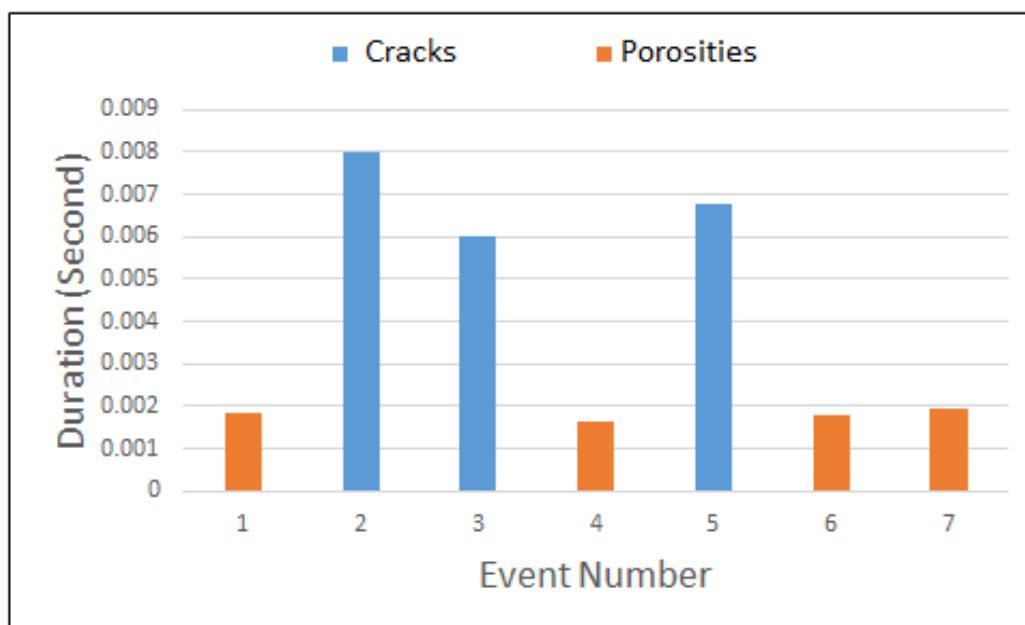
Figure 10 shows waveform samples emitted by a pore and a crack, and it can be seen that the waveform created by a crack is quite different from the waveform from created by a pore. The cracks tend to create AE signals with high energy, longer duration, slower rise time, large number of counts and higher amplitude when compared to the signals generated by porosities.

Table 7. Verification results of the logistic regression analysis and neural network

Event number	Clustering Analysis	LR Probability	ANN
1	Porosity	Porosity	Porosity
2	Crack	Crack	Crack
3	Crack	Crack	Crack
4	Porosity	Porosity	Porosity
5	Crack	Crack	Crack
6	Porosity	Porosity	Porosity
7	Porosity	Porosity	Porosity

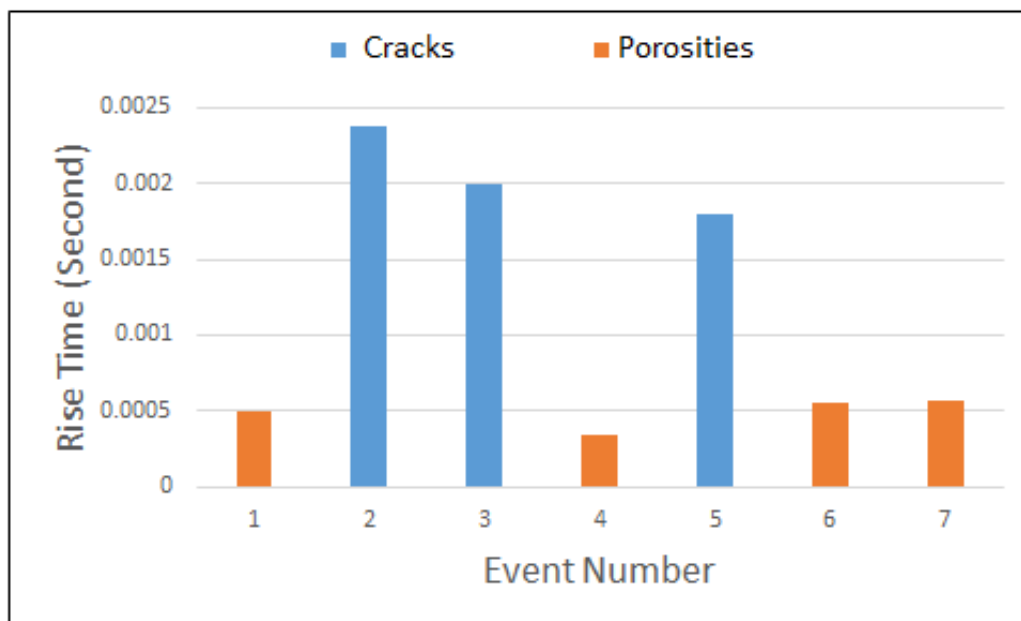


(a) Porosities produce less energy

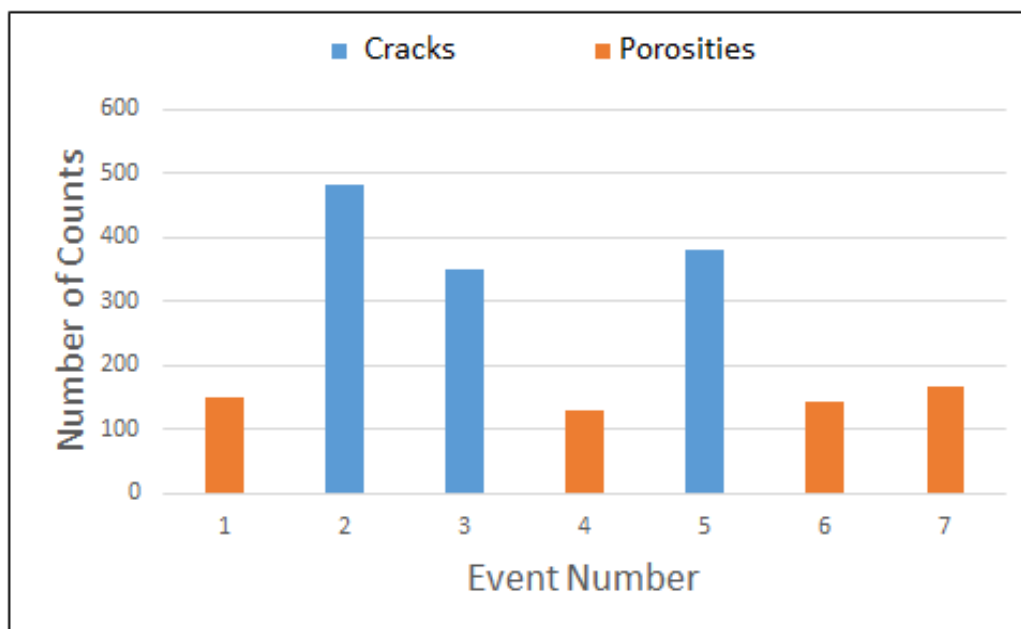


(b) Porosities have shorter duration

Figure 9 . Comparing the signal features between crack and porosities

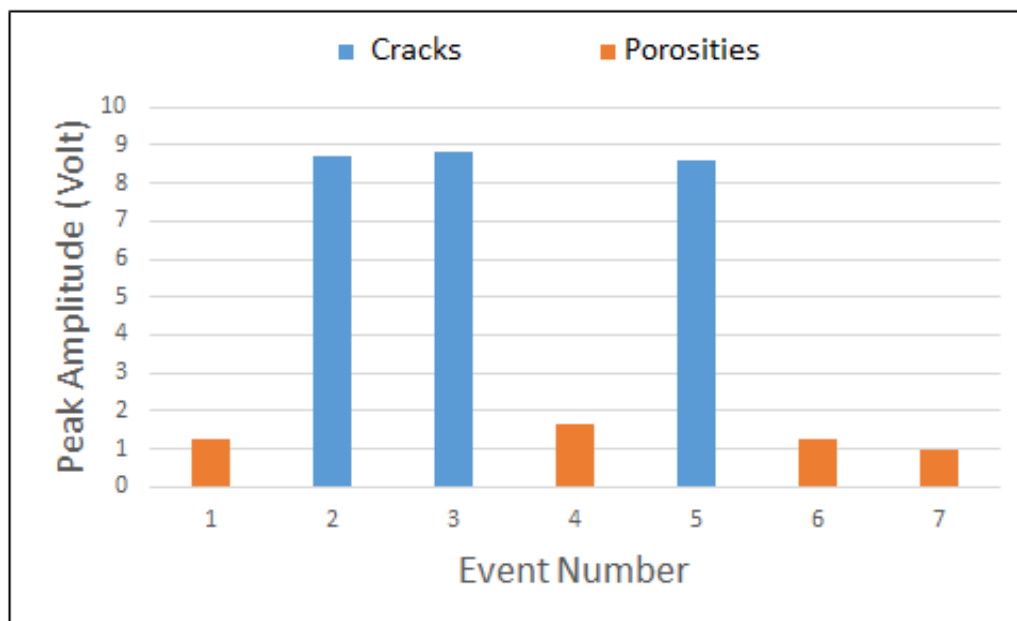


(c) Porosities in have slower rise time



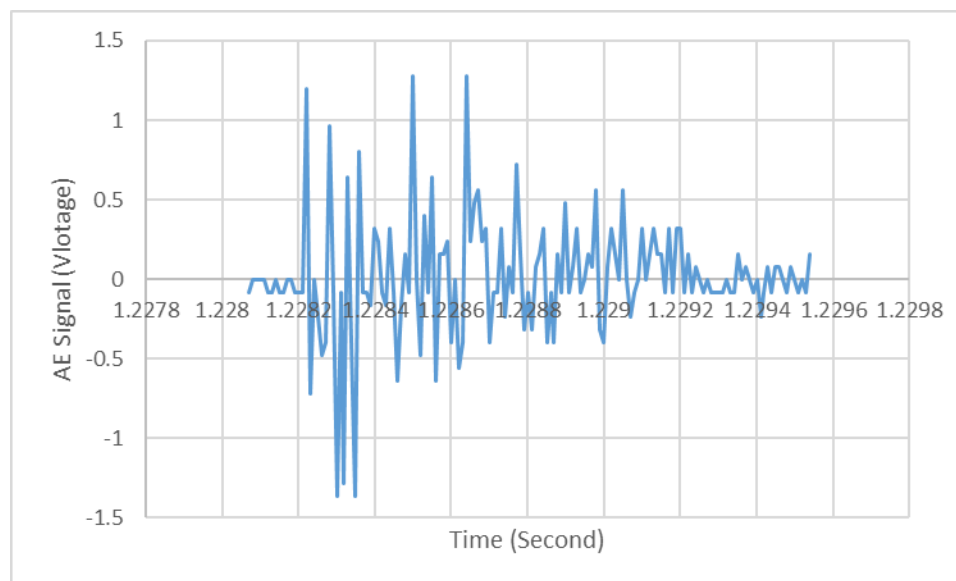
(d) Porosities have less number of counts

Figure 9. Comparing the signal features between crack and porosities (Cont.)



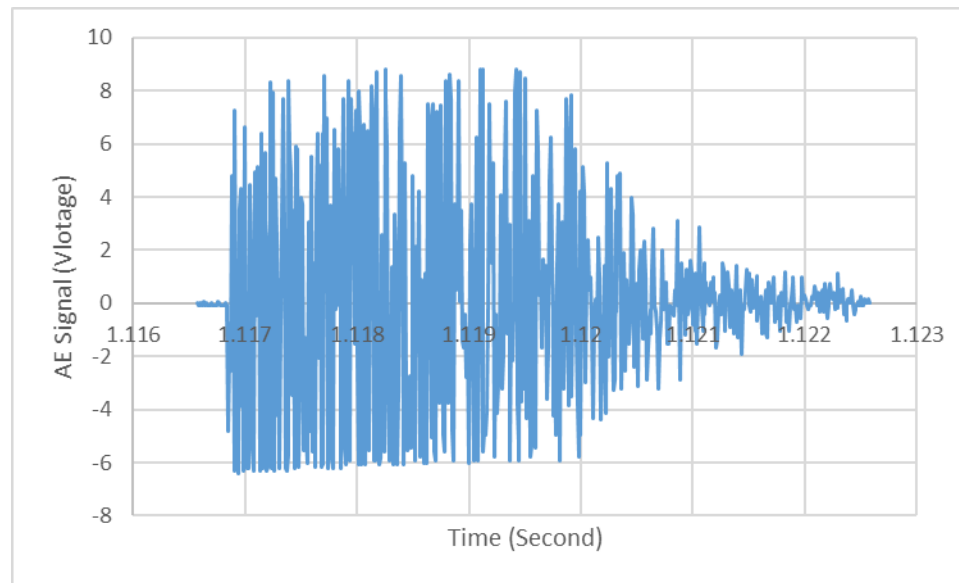
(e) Porosities have lower amplitude

Figure 9. Comparing the signal features between crack and porosities (Cont.)



(a) Waveform signal sample emitted by a pore

Figure 10 . Comparison between the waveforms emitted by cracks and porosities



(b) Waveform signal sample emitted by a crack

Figure 10. Comparison between the waveforms emitted by cracks and porosities (Cont.)

After preparing the surface of the deposited metal, the cracks and pores were observed using an optical microscope. Figure 11 shows cracks caused by thermal stress. During laser deposition, the cracks are formed as result of thermal stress at the combining surface of deposition. The temperature gradient of the deposited layer is higher in the direction of thickness than other directions, and the thermal expansion coefficients are different for the two metal powders, which causes thermal stress. It also occurs with powder contamination in the powder feeder [32].

The second type of observed defect is pores, which have a spherical form and appear in random locations that are not associated with the microstructure, as shown in

Figure 12. The possible sources of these porosities are surface powder contamination [32], gasses trapped within the powder particles due to the difference in the powder sizes,



Figure 11. Optical image of a transverse cross-sectioned laser deposit showing a crack

and an oxidation effect caused by the oxygen level being high due to not using the chamber. In fact, surface oxides may remain in the solid state in the melting pool and, as such, upset the wetting mechanisms that melted the powder and induce voids.

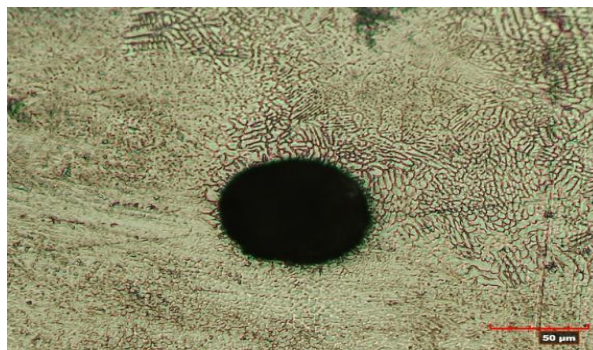


Figure 12. Optical image of a transverse cross-sectioned laser deposit showing a gas porosity

4. CONCLUSIONS

In the presented paper, various types of LMD defects have been evaluated using AE technique. The results of this investigation showed that AE features were influenced by defect presence, and the findings exhibited the capability of AE technology to detect the presence of different defects in the deposited material.

The AE signal was collected during the LMD in an oxidized environment with mixed metal powders in order to stimulate all possible types of defects. Several defects mechanism were activated and detected by AE sensor. An LR model was implemented to analyze the AE signals and identify defects source mechanisms. The results were then compared to the outcomes of an ANN model, and both models demonstrated good agreement with the clustering analysis technique,

According to the logistic regression analysis, the frequency and kurtosis are not significant, which means that they have little contribution to the classification solution, their P-values are greater than 0.05, three out of the seven detected defects are cracks and the rest are pores. The mean squared error of the logistic regression and the neural network models are 1.72973 and 1.702703 respectively, there is an insignificant difference in the performance of the two models.

The LR and ANN successfully distinguished two primary defect types and their signal characteristics. Porosities produced AE signals with shorter decay time and less amplitude, while cracks triggered the AE signals with shorter durations and higher amplitudes, the signal energy is the most significant feature, which means it has the most contribution to the defect classification. AE offers the potential to detect and identify

different LMD defects and thus assess the overall structural health of the part produced by LMD.

ACKNOWLEDGMENT

This research was supported by the National Science Foundation grants IIP-1345240, CMMI-1301414, and CMMI-1547042. Support from Product Innovation and Engineering, LLC, Missouri S&T Intelligent Systems Center, and the Missouri S&T Manufacturing Engineering Program is greatly appreciated.

REFERENCES

- [1] Wang L, Felicelli SD, Craig JE (2009) Experimental and numerical study of the LENS rapid fabrication process. *ASME J Manuf Sci Eng* 131(4):041019-8. doi:[10.1115/1.3173952](https://doi.org/10.1115/1.3173952)
- [2] Weerasinghe VM, Steen WM (1983) Laser cladding by powder injection. In: Chen JMMM Chen, Tucker C (eds) *Transport phenomena in materials processing*, ASME, New York, pp 15–23
- [3] Weerasinghe V, Steen W (1987) Laser cladding with blown powder. *Met Constr* 19:581–585
- [4] Sears JW (1999) Direct laser powder deposition - ‘State of the Art’. No. KAPL-P-000311; K99089 Knolls Atomic Power Lab, Nis, NY
- [5] McLean M (1997) Laser direct casting high nickel alloy components. *Adv Powder Metall Part Mater* 3:21
- [6] Mazumder J, Choi J, Nagarathnam J, Koch K, Hetzner D (1997) The direct metal deposition of H13 tool steel for 3D components. *JOM* 49:55–60
- [7] Lewis G, Nemec R, Milewski J, Thoma D (1994) Directed light fabrication, No. LAUR-94-2845; CONF-9410189-2, Los Alamos Natl. Lab., NM, USA
- [8] Milewski J, Lewis G, Thoma D (1998) Directed light fabrication of a solid metal hemisphere using 5-axis powder deposition. *J Mater Process Technol* 75:165–172

- [9] Wu X, Liang J, Mei J, Mitchell C, Goodwin PS, Voice W (2004) Microstructures of laser-deposited Ti-6Al-4V. *Mater Des* 25:137–144
- [10] Arcella F, Froes F (2000) Producing titanium aerospace components from powder using laser forming. *JOM* 52:28–30
- [11] Fessler JR, Merz R, Nickel AH, Prinz FB (1996) Laser deposition of metals for shape deposition manufacturing. In: *Proceedings of the Solid Freeform Fabrication Symposium, University of Texas, Austin*, pp 117–124
- [12] Keicher DM, Miller WD (1998) LENS moves beyond RP to direct fabrication. *Met Powder Rep* 53:26–28
- [13] Griffith M, Schlienger M, Harwell L (1998) Thermal behavior in the LENS process, No. SAND-98-1850C; CONF-980826. Sandia Natl. Labs, Albuquerque
- [14] Xue L, Islam M (1998) Free-form laser consolidation for producing functional metallic components. *Laser Inst. Am. Laser Mater Process* 84
- [15] Xue L, Islam M (2000) Free-form laser consolidation for producing metallurgically sound and functional components. *J Laser Appl* 12: 160–165
- [16] Ma Z, Sun G, Liu D, Xing X (2016) Dissipativity analysis for discrete-time fuzzy neural networks with leakage and timevarying delays. *Neurocomputing* 175(Part A):579–584
- [17] Gaja H, Liou F (2016) Automatic detection of depth of cut during end milling operation using acoustic emission sensor. *Int J Adv Manuf Technol* 86(9–12):2913–2925
- [18] Duro JA, Padget JA, Bowen CR, Alicia H, Nassehi A (2016) Multi-sensor data fusion framework for CNC machining monitoring. *Mech Syst Signal Process* 66 67:505–520
- [19] Jolly WD (1969) Acoustic emission exposes cracks during welding processes. *Welding J* 48
- [20] Rostek W (1990) Investigations on the connection between the welding process and airborne noise emission in gas shielded metal arc welding. *Schw und Schn* 42(6):E96–E97
- [21] Duley WW, Mao YL (1994) The effect of surface condition on acoustic emission during welding of aluminum with CO₂ laser radiation. *J Phys D Appl Phys* 27:1379

- [22] Grad L, Kralj V (1996) On line monitoring of arc welding process using acoustic signals. In: Proceedings of the 13th Conference BIAM'96, Zagreb, pp i17–i20
- [23] Van SMC, Hermans MJM, Den G (2001) Monitoring of martensite formation during welding by means of acoustic emission. *J Phys D, Appl Phys (UK)* (22):3312–3317
- [24] Grad L, Grum J, Polajnar I, Slabe JM (2004) Feasibility study of acoustic signals for on-line monitoring in short circuit gas metal arc welding. *Int J Mach Tools Manuf* 44(5):555–561
- [25] Yang Z, Yu Z, Wu H, Chang D (2014) Laser-induced thermal damage detection in metallic materials via acoustic emission and ensemble empirical mode decomposition. *J Mater Process Technol* 214(8):1617–1626
- [26] Diego-Vallejo D, Ashkenasi D, Eichler HJ (2013) Monitoring of focus position during laser processing based on plasma emission. *Phys Procedia* 41:911–918
- [27] Wang F, Mao H, Zhang D, Zhao X, Shen Y (2008) Online study of cracks during laser cladding process based on acoustic emission technique and finite element analysis. *Appl Surf Sci* 255 (5, Part 2): 3267–3275
- [28] Siracusano G, Lamonaca F, Tomasello R, Garesci F, La Corter A, Cani DL, Carpentieri M, Grimaldi D, Giovanni F (2016) A framework for the damage evaluation of acoustic emission signals through Hilbert–Huang transform. *Mech Sys Signal Process* 75: 109–122
- [29] Bianchi D, Vernes A (2015) Wavelet packet transform for detection of single events in acoustic emission signals. *Mech Syst Signal Process*
- [30] Gaja H, Liou F (2016) Defects monitoring of laser metal deposition using acoustic emission sensor. *Int J Adv Manuf Technol*:1–14
- [31] Cox DR (1958) The regression analysis of binary sequences. *J R Stat Soc Ser B Methodol* 20(2):251–242
- [32] Barua S (2014) Vision-based defect detection in laser metal deposition process. *Rapid Prototyp J* 20(1):77–85

SECTION

2. CONCLUSIONS

As part of topic one, the main concern of this work was to detect the depth of cut for a part made with a free-form surface process. The depth of cut and the acoustic emission variations were investigated experimentally during end milling of deposited stainless steel 316. A full factorial experimental design was used to conduct experiments. Regression analysis results were compared to the neural network results, and the neural network showed better results in modeling the experimental data. The neural network model was adopted to predict the depth of cut in end milling. The model showed a good agreement between the measured depth of cut by using a 3D scanner and the predicted depth of cut by the artificial neural network model.

In the second topic, The AE signal was collected during the laser metal deposition in an oxidized environment with mixed metal powders to stimulate all possible types of defects. Several defects mechanisms were activated and detected by the AE sensor. K-Means clustering method was implemented to analyze the AE signals and identify defect source mechanisms. Principal components analysis was used to facilitate the visualization of the clusters in 2D and 3D plots. The number of clusters to be created does not have to be specified in advance; they only depend on the number of defects being created. Porosities produce the AE signals with shorter decay time and less amplitude. The cracks trigger the AE signals with short durations and high amplitudes. The signal energy is a crucial feature in identifying the AE defect source mechanisms.

BIBLIOGRAPHY

- [1] Weerasinghe V, Steen W, Laser cladding by powder injection, in: Proc. 1st Int. Conf. Lasers Manuf., 1983, pp. 125–132.
- [2] Weerasinghe V, Steen W, Laser cladding with blown powder, *Met. Constr.* 19 (1987) 581–585.
- [3] Sears JW (1999) Direct laser powder deposition - ‘State of the Art’. No. KAPL-P-000311; K99089 Knolls Atomic Power Lab, Nis, NY
- [4] McLean M (1997) Laser direct casting high nickel alloy components. *Adv Powder Metall Part Mater* 3:21
- [5] Mazumder J, Choi J, Nagarathnam J, Koch K, Hetzner D (1997) The direct metal deposition of H13 tool steel for 3D components. *JOM* 49:55–60
- [6] Lewis G, Nemec R, Milewski J, Thoma D (1994) Directed light fabrication, No. LAUR–94-2845; CONF-9410189–2, Los Alamos Natl. Lab., NM, USA
- [7] Milewski J, Lewis G, Thoma D (1998) Directed light fabrication of a solid metal hemisphere using 5-axis powder deposition. *J Mater Process Technol* 75:165–172
- [8] Wu X, Liang J, Mei J, Mitchell C, Goodwin PS, Voice W (2004) Microstructures of laser-deposited Ti-6Al-4V. *Mater Des* 25:137–144
- [9] Arcella F, Froes F (2000) Producing titanium aerospace components from powder using laser forming. *JOM* 52:28–30
- [10] Fessler JR, Merz R, Nickel AH, Prinz FB (1996) Laser deposition of metals for shape deposition manufacturing. In: *Proceedings of the Solid Freeform Fabrication Symposium*, University of Texas, Austin, pp 117–124
- [11] Keicher DM, Miller WD (1998) LENS moves beyond RP to direct fabrication. *Met Powder Rep* 53:26–28
- [12] Griffith M, Schlienger M, Harwell L (1998) Thermal behavior in the LENS process, No. SAND–98-1850C; CONF-980826. Sandia Natl. Labs, Albuquerque.
- [13] Xue L, Islam M (1998) Free-form laser consolidation for producing functional metallic components. *Laser Inst. Am. Laser Mater Process* 84

- [14] Xue L, Islam M (2000) Free-form laser consolidation for producing metallurgically sound and functional components. *J Laser Appl* 12: 160–165
- [15] Wang L, Felicelli SD, Craig JE (2009) Experimental and Numerical Study of the LENS Rapid Fabrication Process. *ASME. J. Manuf. Sci. Eng.* 2009;131(4):041019-041019-8. doi:10.1115/1.3173952.
- [16] Zhiqiang Ma, Guanghui Sun, Di Liu, Xing Xing (2016) Dissipativity analysis for discrete-time fuzzy neural networks with leakage and time-varying delays, *Neurocomputing*, Volume 175, Part A, Pages 579-584, 29 January 2016.
- [17] Gaja, H., Liou, F. (2016) Automatic detection of depth of cut during end milling operation using acoustic emission sensor. *International Journal of Advanced Manufacturing Technology*, 86 (9-12), pp. 2913-2925.
- [18] Duro JA, Padget JA, Bowen CR, Alicia Kim H, Nassehi A (2016) Multi-sensor data fusion framework for CNC machining monitoring. *Mech Syst Signal Process* 66 67:505–520
- [19] Giulio S, Giovanni F(2016) A framework for the damage evaluation of acoustic emission signals through Hilbert–Huang transform. *Mechanical Systems and Signal Processing*, Volume 75.
- [20] Davide B, Andrés V(2016) Wavelet packet transform for detection of single events in acoustic emission signals. *Mechanical Systems and Signal Processing*, Volumes 64–65, December 2015, Pages 441-451.

VITA

Haythem Gaja received his bachelor's degree in Mechanical Engineering in March 2003 from Tripoli University formerly known as Al fateh University.

In August 2009, he enrolled in the Missouri University of Science and Technology for graduate studies in Manufacturing Engineering. He has been a research assistant under Dr. Frank Liou. He received his master of science in Manufacturing Engineering from Missouri University of Science and Technology in July 2011.

In July 2018, he received his Ph.D. in Electrical Engineering from Missouri University of Science and Technology.